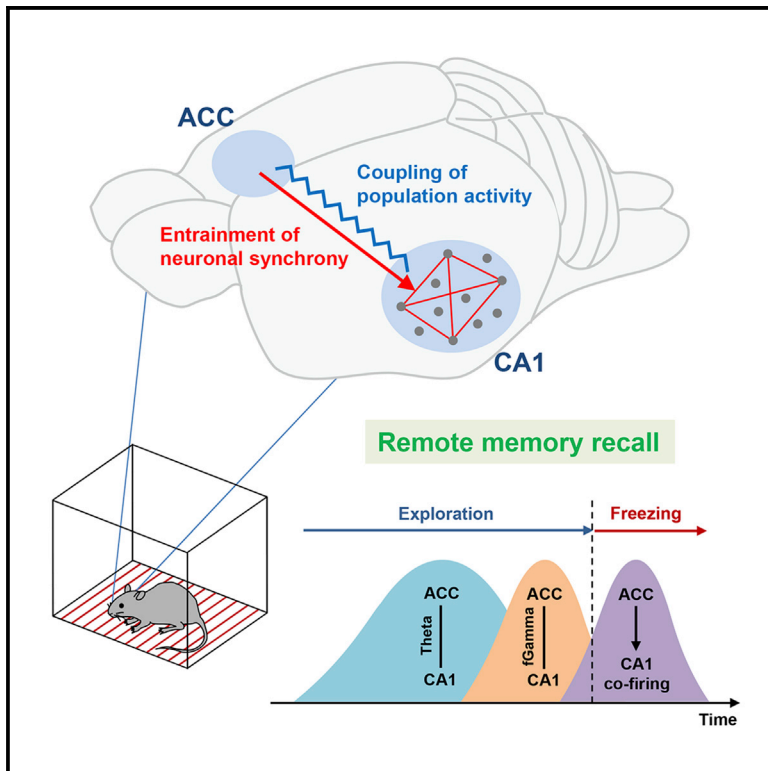


Physiological Signature of Memory Age in the Prefrontal-Hippocampal Circuit

Graphical Abstract



Authors

Yuichi Makino, Denis Polygalov, Federico Bolaños, Andrea Benucci, Thomas J. McHugh

Correspondence

thomas.mchugh@riken.jp

In Brief

Makino et al. demonstrate dynamic electrophysiological interactions between ACC and CA1 during recall of remote contextual fear memory, which result in the reactivation of a sparse population of CA1 neurons. These interactions serve as a signature of memory age that can be decoded by a machine learning classifier.

Highlights

- ACC-CA1 coupling is enhanced during recall of a remote fear memory
- ACC entrains long-distance neuronal synchrony in CA1 during remote recall
- Sequential ACC-CA1 interactions during exploration predict successful remote recall
- The pattern of ACC-CA1 synchronization can accurately decode the age of memory



Physiological Signature of Memory Age in the Prefrontal-Hippocampal Circuit

Yuichi Makino,¹ Denis Polygalov,¹ Federico Bolaños,^{2,3} Andrea Benucci,^{2,3} and Thomas J. McHugh^{1,4,*}¹Laboratory for Circuit and Behavioral Physiology, RIKEN Center for Brain Science, Wakoshi, Saitama 351-0198, Japan²Laboratory for Neural Circuits and Behavior, RIKEN Center for Brain Science, Wakoshi, Saitama 351-0198, Japan³Department of Mathematical Informatics, Graduate School of Information Science and Technology, The University of Tokyo, Tokyo 113-8656, Japan⁴Lead Contact*Correspondence: thomas.mchugh@riken.jp<https://doi.org/10.1016/j.celrep.2019.11.075>

SUMMARY

The long-term storage of episodic memory requires communication between prefrontal cortex and hippocampus. However, how consolidation alters dynamic interactions between these regions during subsequent recall remains unexplored. Here we perform simultaneous electrophysiological recordings from anterior cingulate cortex (ACC) and hippocampal CA1 in mice during recall of recent and remote contextual fear memory. We find that, in contrast to recent memory, remote memory recall is accompanied by increased ACC-CA1 synchronization at multiple frequency bands. The augmented ACC-CA1 interaction is associated with strengthened coupling among distally spaced CA1 neurons, suggesting an ACC-driven organization of a sparse code. This robust shift in physiology permits a support vector machine classifier to accurately determine memory age on the basis of the ACC-CA1 synchronization pattern. Our findings reveal that memory consolidation alters the dynamic coupling of the prefrontal-hippocampal circuit and results in a physiological signature of memory age.

INTRODUCTION

The recall of a memory is thought to engage distinct neural circuits depending on when it was acquired. The standard model argues that memory is initially stored in the hippocampus but then gradually consolidated to the cortex, diminishing the role of the hippocampus in recall (Frankland and Bontempi, 2005; Squire, 1992). This model is supported by the observation that human patients with hippocampal damage show preferential loss of recent memory with relatively intact remote memory (Scoville and Milner, 1957; Squire and Alvarez, 1995). Consistent with this, rodent studies have identified specific cortical regions required for the storage of remote memory, including the prefrontal cortex (Bontempi et al., 1999; Frankland et al., 2004; Kitamura et al., 2017; Maviel et al., 2004).

However, there is accumulating evidence in both rodents and humans that the hippocampus is consistently recruited during recall, irrespective of memory age (Goshen et al., 2011; Mosco-

vitch et al., 2016; Rosenbaum et al., 2000; Winocur and Moscovitch, 2011). Importantly, many of these studies have demonstrated that the hippocampus is required when episodic details of the memory must be retrieved but is dispensable when only coarse information is necessary (Moscovitch et al., 2016; Rosenbaum et al., 2000; Winocur and Moscovitch, 2011). These findings have led to the multiple trace theory, which states that the hippocampus is permanently involved in storage and retrieval of detailed episodic information, while semantic (gist) information is established in the cortex and can survive damage to the hippocampus (Moscovitch et al., 2016; Winocur and Moscovitch, 2011; Winocur et al., 2010). The prefrontal cortex and hippocampus are anatomically connected, both directly and indirectly, raising the possibility that there may be a dynamic interplay between the two types of information they carry during retrieval of remote memory (Eichenbaum, 2017; Winocur et al., 2010). Nonetheless, it remains unclear if the recall of remote memory has a distinct physiological signature that reflects the shift in the interactions between the regions and how it may be associated with the neuronal activity underlying recall.

To address this question, we investigated the dynamic electrophysiological interactions between the prefrontal cortex and hippocampus during recall of remote memory. We performed simultaneous local field potential (LFP) and single-unit recordings from the anterior cingulate cortex (ACC) and dorsal CA1 region in mice, areas repeatedly implicated in remote memory storage and recall (Bontempi et al., 1999; Frankland et al., 2004; Goshen et al., 2011; Maviel et al., 2004). We found that ACC synchronizes with CA1 at multiple frequencies during remote memory recall, accompanied by an increase in the synchronous firing of distally spaced CA1 neurons. In addition, the shifts in ACC-CA1 interactions from recent to remote memory were robust enough to be used to classify the age of memory.

RESULTS

ACC-CA1 Theta Synchrony Is Increased during Recall of Remote Memory

We designed a multi-tetrode microdrive to simultaneously record both single-unit activity and LFP from ACC and CA1 in freely behaving mice (additional tetrodes targeted the basolateral amygdala [BLA]; see STAR Methods). After surgery, baseline neuronal activity was recorded as the mice explored a chamber that was later used for contextual fear conditioning (CFC). Mice



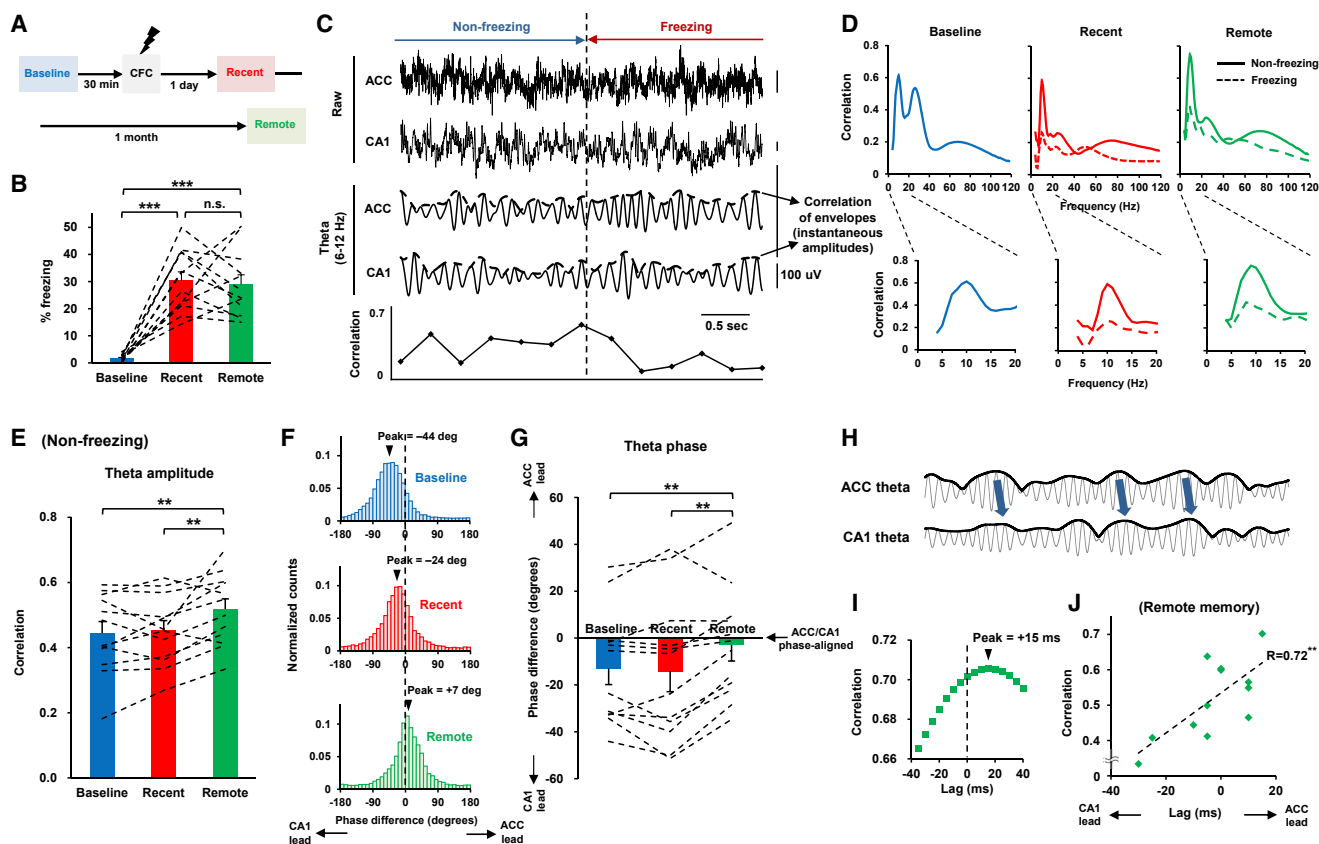


Figure 1. ACC-CA1 Theta Synchrony Is Enhanced during the Remote Memory Recall Session

(A) Experimental timeline. During the baseline session, mice were placed in the contextual fear conditioning (CFC) chamber, and activity in ACC and CA1 was recorded for 10 min. Following conditioning, mice were returned to the CFC chamber 1 day (recent) and 1 month (remote) later and activity was recorded for 10 min during fear memory recall.

(B) Freezing during the baseline, recent, and remote sessions ($F_{2,22} = 36.91$, $p < 0.001$; baseline versus recent, $p < 0.001$; baseline versus remote, $p < 0.001$; recent versus remote, $p = 0.938$).

(C) Representative raw and theta-filtered local field potentials (LFPs) at ACC and CA1 during remote session, with instantaneous amplitudes (envelopes) of theta-filtered LFP overlaid (dotted line). Correlation of instantaneous amplitudes from the two regions is shown at the bottom. The vertical dotted line indicates the transition point from non-freezing to freezing.

(D) Representative ACC-CA1 instantaneous amplitude correlation at different frequencies for baseline, recent, and remote sessions and for non-freezing and freezing periods, respectively, all taken from the same mouse. Expanded curve in the theta range is shown below each plot.

(E) Mean ACC-CA1 instantaneous amplitude correlation at theta frequency during non-freezing periods over all mice is shown for baseline, recent, and remote sessions ($F_{2,22} = 9.05$, $p = 0.001$; baseline versus recent, $p = 0.914$; baseline versus remote, $p = 0.002$; recent versus remote, $p = 0.006$).

(F) Representative distributions of phase differences between ACC theta and CA1 theta during non-freezing periods.

(G) Phase difference between ACC theta and CA1 theta during non-freezing periods ($F_{2,22} = 9.62$, $p < 0.001$; baseline versus recent, $p = 0.900$; baseline versus remote, $p = 0.005$; recent versus remote, $p = 0.002$).

(H) For non-freezing periods of remote memory session, one of the LFPs was shifted, and the LFP-LFP time lag was calculated where theta instantaneous amplitude correlation was maximum.

(I) Representative lag-correlation plot, where the time lag resulting in the maximum correlation is indicated by an arrowhead.

(J) Correlation between the time lag with the strength of ACC-CA1 theta correlation over individual mice ($R = 0.72$, $p = 0.004$).

In (B), (E), and (G), $n = 12$ mice, within-subject ANOVA with post hoc comparisons using Tukey's honestly significant difference (HSD) test. In (J), $n = 12$ mice, test of no correlation. For all bar graphs, data are represented as mean \pm SEM, and dotted lines indicate values from individual mice. ** $p < 0.01$ and *** $p < 0.001$.

See also [Figures S1–S5](#).

then underwent CFC training, leading to formation of a long-lasting contextual fear memory. The animals were brought back to the same CFC chamber 1 day (recent memory) and 1 month (remote memory) following CFC, and neural activity was recorded as memory was assessed by scoring time spent freezing ([Figure 1A](#)). Placement of tetrodes in ACC and CA1 was confirmed after the experiment ([Figure S1A](#)).

Mice exhibited similar levels of freezing during recent memory and remote memory sessions ([Figure 1B](#)), indicating that our behavioral protocol resulted in a stable long-lasting fear memory. To contrast ACC-CA1 interactions during recent and remote recall with activity during the baseline session prior to conditioning, we examined the correlation of instantaneous LFP amplitudes (correlation of envelopes; [Figure 1C](#)), an approach

used to measure the strength and direction of cross-regional interaction of population activity during behavior (Adhikari et al., 2010; Likhtik et al., 2014; Place et al., 2016). To control for state-dependent changes and allow comparison with the baseline session during which freezing was rare, we analyzed freezing and non-freezing periods separately (Figure 1C) and focused primarily on non-freezing periods to permit comparison across all sessions.

We first examined the ACC-CA1 correlation in the theta band (6–12 Hz; Figure 1C), as prefrontal-hippocampal interactions in this range have been implicated in various aspects of behavior (Eichenbaum, 2017; Place et al., 2016). Consistent with this, across all frequencies and in all sessions the most robust ACC-CA1 correlation during non-freezing periods was observed at theta (Figure 1D). Comparing across sessions revealed that ACC-CA1 theta correlation during non-freezing periods was significantly higher during the remote memory session compared with the recent memory and baseline sessions (Figure 1E). The increase of theta correlation during the remote session was not observed during freezing periods (Figures S2A and S2B), suggesting that it may be involved in the initiation of the recall process during exploration, which exposes mice to memory-associated cues. Also, the increased theta correlation was not seen during habituation sessions performed immediately prior to the baseline, recent, and remote session (Figure S3A), demonstrating that it was not a simple time-dependent change. The increased theta correlation was not due to a change in theta power, which remained consistent in both regions across sessions (Figure S1B). Furthermore, both theta phase alignment (Figures 1F and 1G) and coherence (Figure S1C) between ACC and CA1 significantly increased during the remote session, providing additional evidence of enhanced ACC-CA1 interaction during remote memory recall.

To better understand if the increased ACC-CA1 synchrony during the remote session reflected behavioral changes in non-freezing periods, we next examined the relationship of this physiological change to more specific behavioral states. We first dissected detailed behavioral patterns using the DeepLabCut algorithm to track multiple points on each mouse across every session (Mathis et al., 2018). The automated tracking revealed higher velocities of each tracked point during the baseline session, but no differences between recent and remote sessions (Figures S4A and S4B), consistent with the lack of freezing prior to training. These multipoint tracking data were then used to assign frames to distinct behavioral states that were consistent across sessions and explained the majority of the data: exploration, head movement and freezing (see STAR Methods). Comparison of the duration or frequency of these substates during non-freezing periods again showed no differences between the recent and remote recall session (Figure S4C). Next, to ask if the increased ACC-CA1 theta correlation was observed in a specific substate, we reanalyzed the physiology and found a robust increase during remote session exploration periods (Figure S4D), suggesting that this effect is not related to gross changes in behavior across time. Furthermore, tracking of the mouse's head with higher temporal resolution (30 Hz) again revealed comparable velocities during non-freezing periods between recent and remote sessions (Figures S5A and S5B), and

the enhanced ACC-CA1 theta correlation was still observed when the analysis was limited to specific velocity ranges (Figure S5C). These observations support the idea that the increased ACC-CA1 theta synchrony at the remote session is specifically associated with memory recall but not changes in behavior.

To examine if the enhanced ACC-CA1 theta correlation was directional, we calculated the temporal lag between instantaneous theta amplitudes of ACC and CA1 that generated the maximum correlation (Adhikari et al., 2010; Likhtik et al., 2014; Place et al., 2016). Mice with higher ACC-CA1 theta correlation exhibited more ACC-to-CA1 directional influence (Figures 1H–1J), which was confirmed by Granger causality analysis (Figure S1D). Together, these results suggest that ACC provides a top-down signal during remote memory recall.

Remote Memory Recall Induces Cross-Frequency Coupling to Enhance ACC-CA1 Gamma Synchrony

Similar to theta, long-range interactions at gamma frequency have been reported to mediate memory-related behavioral processes (Buzsáki and Wang, 2012). To test if long-range gamma interaction is involved in remote memory, we examined LFP instantaneous amplitude correlation between ACC and CA1 at both slow-gamma and fast-gamma frequencies (Figure 2A), which have been shown to reflect distinct neural and behavioral processes (Buzsáki and Wang, 2012; Colgin et al., 2009; Middleton and McHugh, 2016). Frequency-correlation curves showed clear local peaks in the fast-gamma range (60–90 Hz), but not in the slow-gamma range (30–50 Hz), during non-freezing periods of all sessions (Figure 1D), with a significant increase observed during the remote recall session (Figure 2B). Again, the increased fast-gamma correlation was not due to a time-dependent change (Figure S3A), a change of fast-gamma power in either region (Figure S1B), behavioral substate (Figure S4D), or velocity (Figure S5C). Furthermore, both slow-gamma and fast-gamma correlations were comparable between recent and remote memory sessions during freezing periods (Figure S2B), suggesting a specific involvement of the increased fast-gamma interaction in the exploration-driven recall of remote memory.

Because the amplitude of gamma oscillations is modulated by theta phase (cross-frequency phase-amplitude coupling) in some brain regions, including the hippocampus (Buzsáki and Wang, 2012; Colgin et al., 2009; Middleton and McHugh, 2016), we next inquired if the change of ACC-CA1 fast-gamma interaction during remote recall was coordinated by theta activity. Fast-gamma amplitude in both CA1 and ACC was robustly modulated by the phase of ACC theta during non-freezing periods, but amplitude of slow-gamma was not (Figure 2C). Strikingly, the modulation strength of ACC theta phase on CA1, but not ACC, fast-gamma amplitude significantly increased during the remote session (Figure 2D). The modulation of CA1 fast-gamma by ACC theta remained unchanged during the habituation session (Figure S3B) and was unaffected by behavioral substate (Figure S4E) or velocity (Figure S5D), suggesting a specific involvement in recall. We found no time-dependent change in the modulation of ACC fast-gamma by CA1 theta (Figure S1E), suggesting that the cross-regional fast-gamma entrainment is

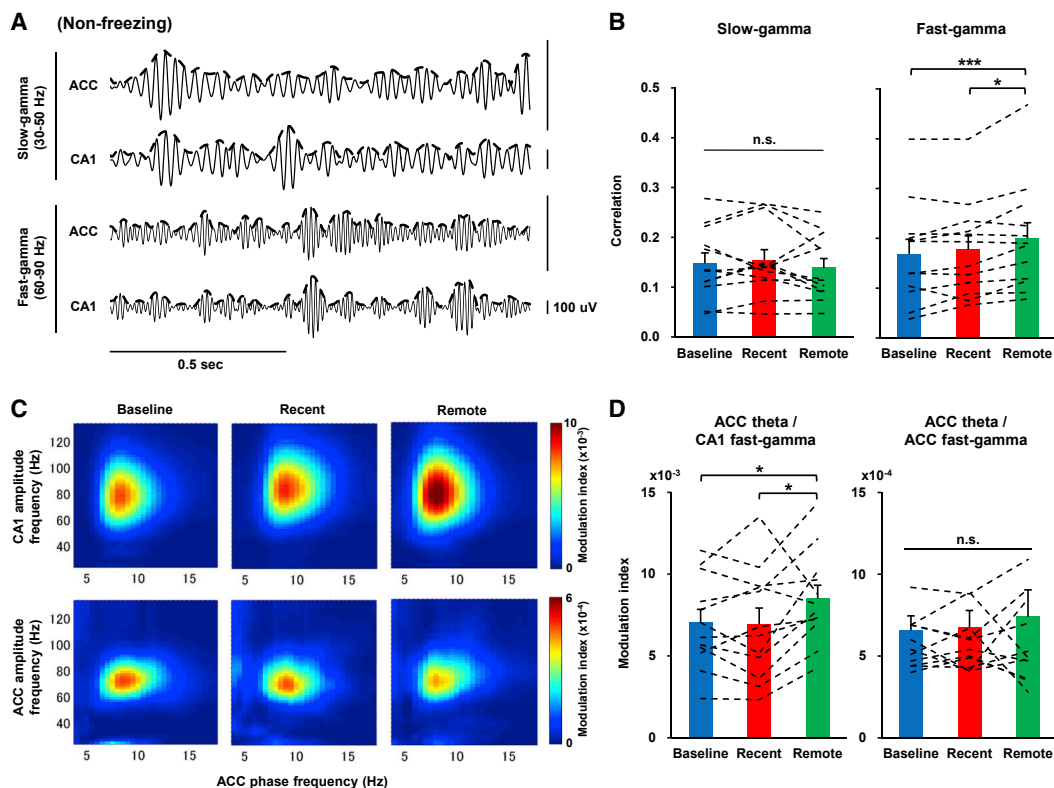


Figure 2. ACC-CA1 Fast-Gamma Synchrony and Cross-Frequency Coupling Are Increased during the Remote Recall Session

(A) Representative LFP traces at ACC and CA1 filtered both at slow-gamma and fast-gamma frequencies.

(B) ACC-CA1 instantaneous amplitude correlations at slow-gamma and fast-gamma frequencies during non-freezing periods (slow-gamma: $F_{2,22} = 1.01$, $p = 0.382$; fast-gamma: $F_{2,22} = 10.69$, $p < 0.001$; baseline versus recent, $p = 0.432$; baseline versus remote, $p < 0.001$; recent versus remote, $p = 0.011$).

(C) Representative cross-frequency phase-amplitude comodulograms during non-freezing periods for baseline, recent, and remote sessions, respectively, all taken from the same mouse. Strength of modulations of ACC LFP amplitude and of CA1 LFP amplitude by ACC LFP phase is indicated by modulation index (see STAR Methods for details). Note that the color scale is different between the upper and lower panels.

(D) Modulation index of fast-gamma amplitude in ACC and in CA1 by ACC theta phase during non-freezing periods (CA1 fast-gamma: $F_{2,22} = 4.78$, $p = 0.019$; baseline versus recent, $p = 0.987$; baseline versus remote, $p = 0.042$; recent versus remote, $p = 0.030$; ACC fast-gamma: $F_{2,22} = 0.66$, $p = 0.526$). Note that the scale is 10 times greater in the left panel.

In (B) and (D), $n = 12$ mice, within-subject ANOVA with post hoc comparisons using Tukey's HSD test. For all bar graphs, data are represented as mean \pm SEM, and dotted lines indicate values from individual mice. * $p < 0.05$ and *** $p < 0.001$.

See also Figures S1–S5.

unidirectional from ACC to CA1. Together these data demonstrate that remote memory recall is associated with enhanced fast-gamma synchrony between ACC and CA1, likely organized by increased modulation of CA1 fast-gamma activity by ACC theta.

ACC Coordinates CA1 Neuronal Activity during Remote Memory Recall

Having observed that ACC-CA1 LFP interactions are augmented during recall of remote memory, we next asked if memory age induces differential cross-regional influence at the level of individual neurons. Previous studies have shown that cross-regional phase-locking of neuronal activity to LFP oscillation underlies various behaviors (Siapas et al., 2005; Sigurdsson et al., 2010). To explore how CA1 neuronal activity is coordinated by ACC, we analyzed cross-regional phase-locking of CA1 single-unit activity to ACC theta (Figures 3A and 3B). We found that the

phase-locking strength of CA1 neurons to ACC theta during non-freezing periods significantly increased during the remote session compared with the baseline and recent session (Figure 3C, left), and this increase was not observed during the habituation session prior to recall (Figure S3C). In contrast, the phase-locking strength of ACC neurons to ACC theta and to CA1 theta remained unchanged (Figure 3C, right; Figure S1F), suggesting that the cross-regional entrainment of spike activity is unidirectional from ACC to CA1. Notably, the increased phase-locking of CA1 neurons to ACC theta was also observed during freezing (Figure S2C), possibly reflecting ongoing memory recall across both states.

We next asked if neuronal output is changed in CA1 and ACC during remote memory recall. Firing rates across the entire neuronal populations in CA1 and ACC were comparable among baseline, recent, and remote sessions (Figure 3D). However, the subpopulation of CA1 neurons that were significantly phase-

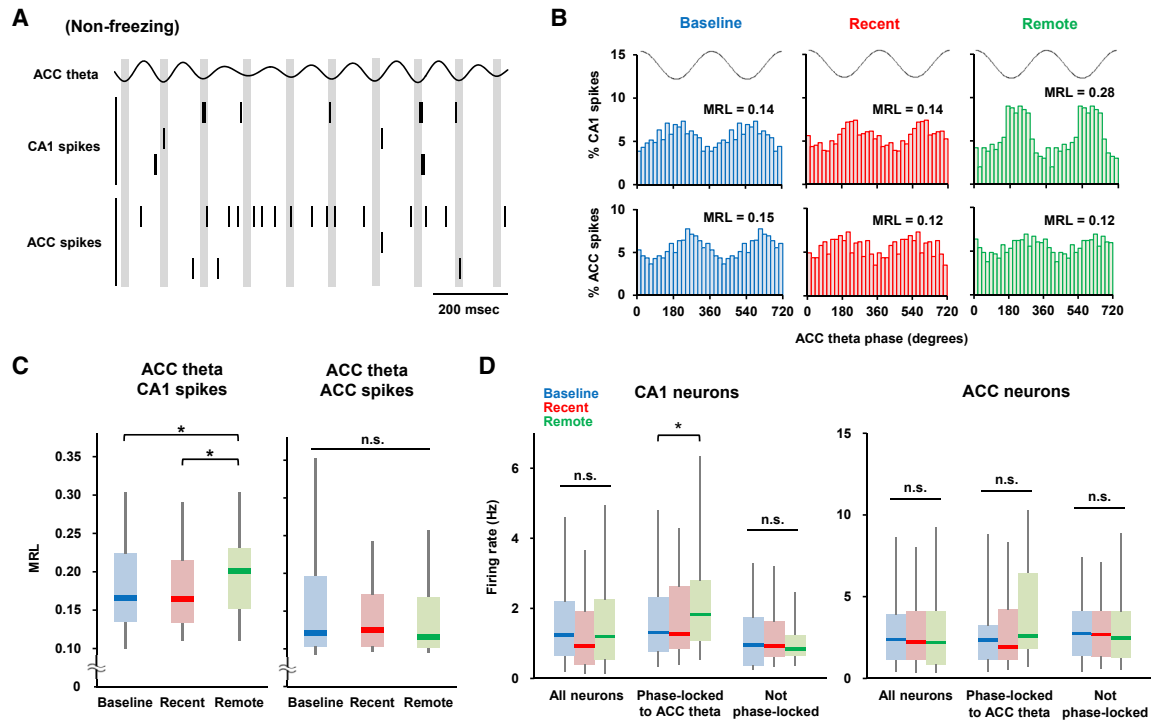


Figure 3. ACC Theta Activity Entrainment of CA1 Neuronal Firings during the Remote Recall Session

(A) Representative ACC LFP filtered at theta frequency (6–12 Hz) along with three simultaneously recorded neurons in each of CA1 and ACC. Shaded lines indicate theta troughs.

(B) Spike probability in CA1 and ACC across ACC theta phase. Replicates of data from 0°–360° are shown at 360°–720° to make the rhythmicity clearer. Mean resultant length (MRL), an index of the strength of phase-locking, is shown for each neuron.

(C) MRL of CA1 and ACC neurons that are significantly phase-locked to ACC theta ($p < 0.05$, Rayleigh test) is shown for non-freezing periods in the baseline, recent, and remote sessions (CA1 spikes: $n = 123$ [baseline], 77 [recent], and 76 [remote] neurons; $H = 7.60$, $p = 0.022$; baseline versus recent, $p = 0.959$; baseline versus remote, $p = 0.039$; recent versus remote, $p = 0.042$; ACC spikes: $n = 40$ [baseline], 33 [recent], and 24 [remote] neurons; $H = 0.14$, $p = 0.931$).

(D) Firing rates during non-freezing periods of the entire CA1 and ACC neuronal populations as well as of the subpopulations that are and are not phase-locked to ACC theta (CA1, all neurons: $n = 144$ [baseline], 140 [recent], and 115 [remote] neurons; $H = 5.15$, $p = 0.076$; CA1, phase-locked: $n = 123$ [baseline], 77 [recent], and 76 [remote] neurons; $H = 6.04$, $p = 0.049$; baseline versus recent, $p = 0.654$; baseline versus remote, $p = 0.041$; recent versus remote, $p = 0.287$; CA1, not phase-locked: $n = 17$ [baseline], 33 [recent], and 15 [remote] neurons; $H = 0.24$, $p = 0.886$; ACC, all neurons: $n = 78$ [baseline], 95 [recent], and 65 [remote] neurons; $H = 0.13$, $p = 0.936$; ACC, phase-locked: $n = 40$ [baseline], 33 [recent], and 24 [remote] neurons; $H = 1.67$, $p = 0.434$; ACC, not phase-locked: $n = 36$ [baseline], 58 [recent], and 35 [remote] neurons; $H = 0.15$, $p = 0.927$).

In (C) and (D), Kruskal-Wallis test with post hoc comparisons using Steel-Dwass test, neurons recorded from 13 (baseline), 13 (recent), and 12 (remote) mice. For all box plots, the middle, bottom, and top lines correspond to the median, lower and upper quartiles, and the edges of lower and upper whiskers correspond to the 5th and 95th percentiles, respectively. * $p < 0.05$.

See also Figures S1–S3 and S5.

locked to ACC theta demonstrated a significantly higher firing rate during the remote session, while CA1 neurons not phase-locked to ACC theta showed no increase (Figure 3D). This was again not observed during the habituation session (Figure S3D) and was not seen in the ACC, in which both phase-locked and non-phase-locked neurons exhibited comparable firing rates across sessions (Figure 3D). These results suggest that ACC may coordinate CA1 neuronal activity during remote memory recall to facilitate retrieval of contextual detail stored in CA1 neurons (Moscovitch et al., 2016; Winocur and Moscovitch, 2011; Winocur et al., 2010).

To explore whether these changes of CA1 spiking activity during the remote session reflect altered recognition of the spatial environment by individual neurons, we analyzed CA1 place cells (Figure S5E). We found no differences in firing rate

or spatial information of pyramidal cells across sessions, but we did observe a similar reduction in place field size in recent and remote sessions compared with baseline (Figures S5F–S5I), most likely because of the more limited chamber exploration accompanying freezing behavior. This suggests that an increased entrainment by ACC on CA1 neurons, but not altered spatial coding by CA1 neurons themselves, may mediate recall of remote memory.

Co-firing of Long-Distance CA1 Neuronal Pairs Entrained by ACC Reflects Successful Remote Memory Recall

The increased entrainment of CA1 neuronal activity by ACC theta during the remote session may provide temporal organization across the CA1 population, potentially generating synchronous

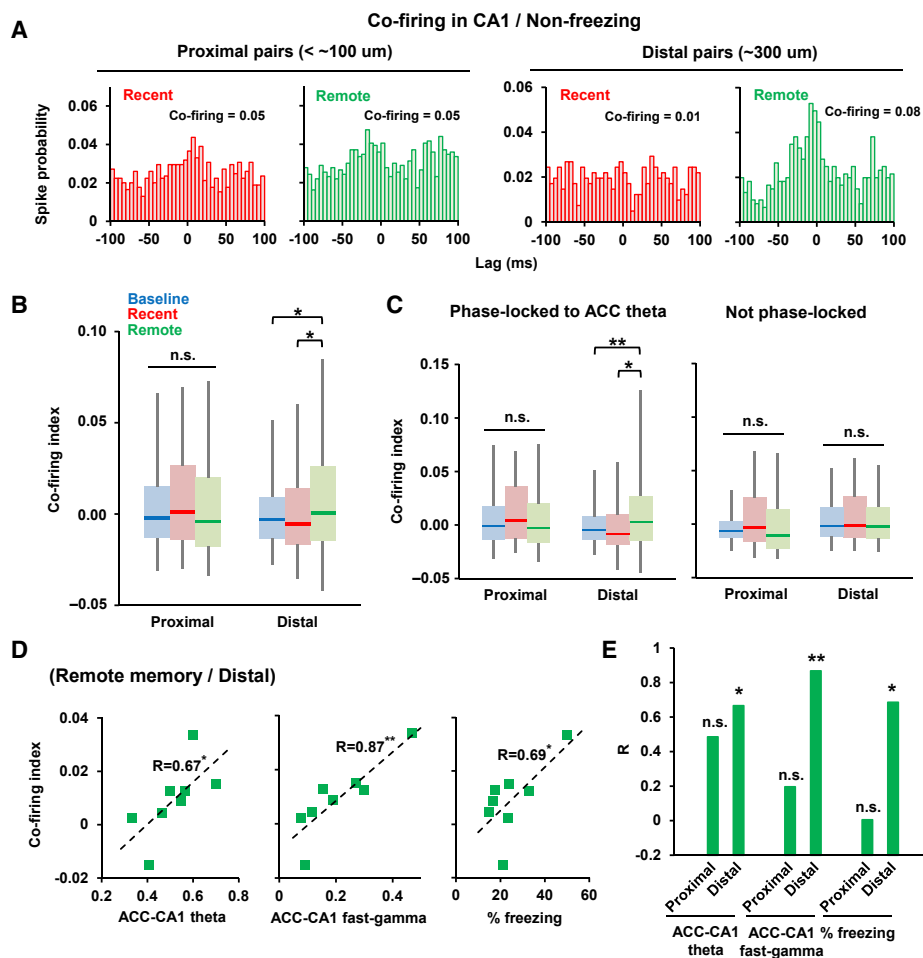


Figure 4. ACC Entrains Long-Distance Co-firing in CA1 during Successful Remote Memory Recall

(A) Representative cross-correlograms of neuron pairs in CA1 recorded from the same tetrodes (proximal; two neurons are located within approximately 100 μ m of each other) and different tetrodes (distal; located approximately 300 μ m apart). Co-firing index (count of spike coincidences within 10 ms normalized by firing rates of the two neurons, with epoch-shuffled values subtracted; see STAR Methods for details) is shown for each neuron pair.

(B) Population average of CA1 co-firing index during non-freezing periods for both proximal and distal neuron pairs (proximal: $n = 326$ [baseline], 143 [recent], and 159 [remote] neuron pairs; $F_{2,625} = 1.50$, $p = 0.224$; distal: $n = 316$ [baseline], 133 [recent], and 160 [remote] neuron pairs; $F_{2,606} = 4.52$, $p = 0.011$; baseline versus recent, $p = 1.000$; baseline versus remote, $p = 0.012$; recent versus remote, $p = 0.046$).

(C) Co-firing for CA1 neuron pairs that are both phase-locked to ACC theta significantly ($p < 0.05$) and that for the rest of CA1 neuron pairs (phase-locked and proximal: $n = 244$ [baseline], 84 [recent], and 134 [remote] neuron pairs; $F_{2,459} = 1.16$, $p = 0.314$; phase-locked and distal: $n = 239$ [baseline], 74 [recent], 120 [remote] neuron pairs; $F_{2,430} = 5.68$, $p = 0.004$; baseline versus recent, $p = 0.849$; baseline versus remote, $p = 0.007$; recent versus remote, $p = 0.015$; not phase-locked and proximal: $n = 82$ [baseline], 59 [recent], and 25 [remote] neuron pairs; $F_{2,163} = 1.09$, $p = 0.339$; not phase-locked and distal: $n = 77$ [baseline], 59 [recent], 40 [remote] neuron pairs; $F_{2,173} = 0.03$, $p = 0.969$).

(D) Correlations of CA1 co-firing index (averaged per mouse) with ACC-CA1 instantaneous amplitude correlation at theta and fast-gamma frequencies, and with percentage freezing, respectively. Results from remote session, during non-freezing periods, and for distal neuron pairs are shown. Only the mice with at least three neuron pairs were included in the analysis.

(E) Summary of the correlation analysis described in (D). Correlations for both proximal and distal neuron pairs are shown (theta and proximal: $R = 0.49$, $p = 0.135$; theta and distal: $R = 0.67$, $p = 0.036$; fast-gamma and proximal: $R = 0.20$, $p = 0.337$; fast-gamma and distal: $R = 0.87$, $p = 0.003$; percentage freezing and proximal: $R = 0.01$, $p = 0.496$; percentage freezing and distal: $R = 0.69$, $p = 0.030$).

In (B) and (C), between-subjects ANOVA with post hoc comparisons using Tukey's HSD test, neurons recorded from 13 (baseline), 13 (recent), and 12 (remote) mice. In (D) and (E), $n = 7$ mice for proximal and 8 mice for distal, test of no correlation. For all box plots, the middle, bottom, and top lines correspond to the median, lower and upper quartiles, and the edges of lower and upper whiskers correspond to the 5th and 95th percentiles, respectively. * $p < 0.05$ and ** $p < 0.01$. See also Figures S2, S3, and S6.

neuronal activity supporting memory retrieval (Cheng and Frank, 2008; Rajasetupathy et al., 2015). To address this, we examined the co-firing of neuronal pairs in CA1 during non-freezing periods (Figure 4A). Pairs of CA1 neurons that were recorded

on the same tetrode ("proximal"; estimated to be within ~ 100 μ m of each other [Buzsáki, 2004]) showed comparable levels of co-firing across all sessions (Figure 4B, left). However, CA1 neuronal pairs that were recorded from different tetrodes

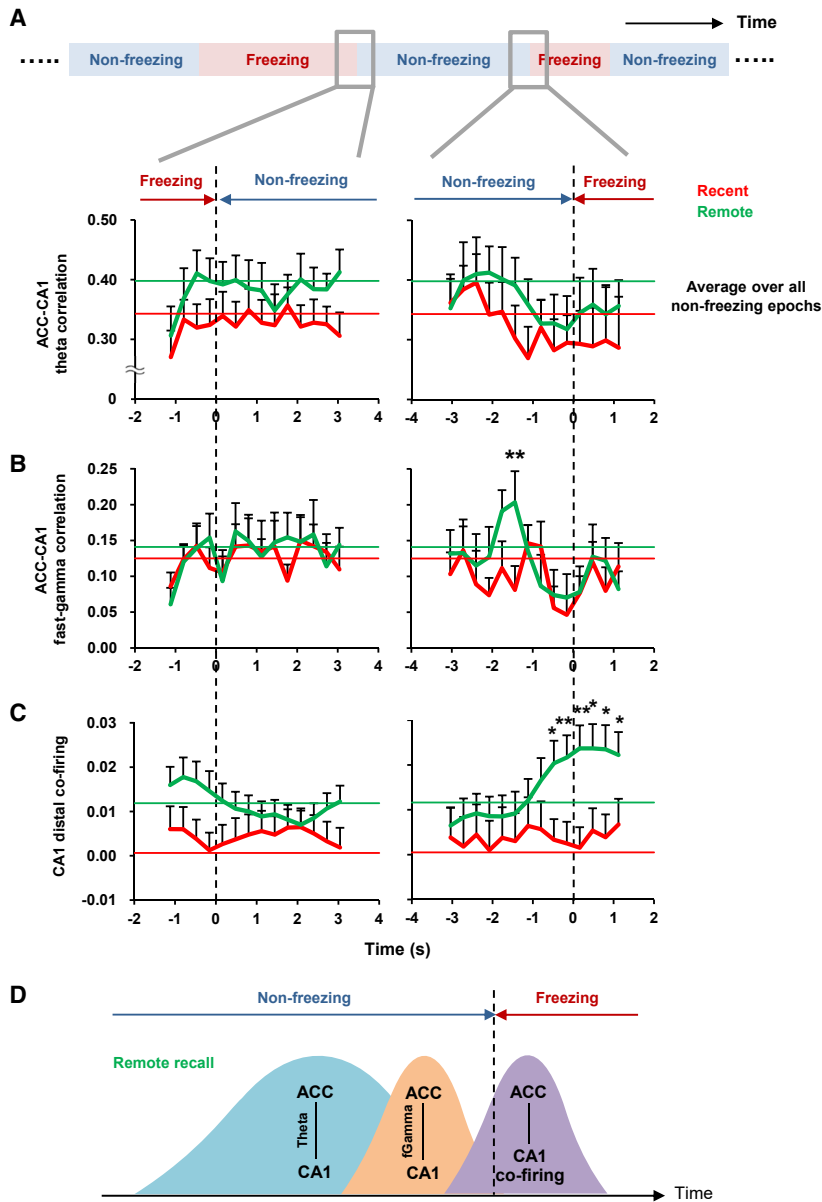


Figure 5. A Temporal Sequence of ACC-CA1 Interactions Precede the Onset of Freezing during the Remote Recall Session

(A) ACC-CA1 instantaneous amplitude correlation at theta frequency was calculated every 0.32 s immediately before and after the onset (left) and offset (right) of freezing. Average correlation values over all non-freezing periods are shown by horizontal lines.

(B) ACC-CA1 instantaneous amplitude correlation at fast-gamma frequency was calculated around the freezing onset and offset.

(C) Co-firing index of CA1 distal neuron pairs that are both phase-locked to ACC theta was calculated around the freezing onset and offset (left: $n = 119$ [recent] and 163 [remote] neuron pairs; right: $n = 110$ [recent] and 159 [remote] neuron pairs).

(D) A temporal sequence model of ACC-CA1 interaction underlying remote memory recall. See Discussion for details.

In (A) and (B), $n = 12$ mice, two-tailed within-subject t test for each time point. In (C), two-tailed between-subject t test for each time point, neurons recorded from 13 (recent) and 12 (remote) mice. For all line plots, data are represented as mean \pm SEM. * $p < 0.05$ and ** $p < 0.01$ between the recent and remote sessions.

firing during the remote session was due to altered ripple occurrence. We detected ripple events in CA1 during non-freezing periods (Figure S6E) and found no changes in the occurrence of ripple events or the associated large irregular activity across sessions (Figures S6F and S6H). In addition, the increased distal co-firing was still observed after removing the spikes within ripple events (Figure S6G), indicating that spike synchrony outside ripple events is enhanced during the remote session.

To explore whether the increased CA1 co-firing was influenced by the ACC, we compared the co-firing of CA1 neuron pairs that were both phase-locked to ACC theta with the remainder of the pairs. The increased co-firing during the remote session was

observed specifically for distally located CA1 neuron pairs that were both phase-locked to ACC (Figure 4C), suggesting that ACC organizes this CA1 long-distance co-firing. The increased distal co-firing at the remote time point was not observed during the habituation session either for the entire CA1 population or for the subpopulation phase-locked to ACC theta (Figure S3E), again excluding the possibility of a simple time-dependent change. Notably, when we limited the analysis to the phase-locked pairs with top 50 or 20 percent of co-firing index in each the session, the increase during the remote session was even more robust (Figure S6I), raising the possibility that only a subpopulation of CA1 neurons are involved in these changes. Furthermore, mice with higher co-firing of distal CA1 neuron pairs also demonstrated larger ACC-CA1 theta and fast-gamma instantaneous amplitude correlations, as well as increased

(“distal”; positioned ~ 300 μm apart; Figure S6A) demonstrated significantly increased co-firing during the remote memory session (Figure 4B, right). This increase was observed with multiple indices, both with and without subtraction of epoch-shuffled values and across various time bins (Figure S6B), suggesting an actual increase of coincidence and not non-specific changes, such as altered firing rate. Also, co-firing was uncorrelated with the quality of single-unit isolation (Figures S6C and S6D), excluding the possibility of spurious co-firing caused by spike misclustering (Quirk and Wilson, 1999). The increased co-firing of distally spaced neurons was also observed during freezing periods (Figure S2D), potentially supporting the persistence of memory recall.

To ensure that these changes were not related to changes in physiological state (Buzsáki, 2015), we asked if CA1 distal co-

observed specifically for distally located CA1 neuron pairs that were both phase-locked to ACC (Figure 4C), suggesting that ACC organizes this CA1 long-distance co-firing. The increased distal co-firing at the remote time point was not observed during the habituation session either for the entire CA1 population or for the subpopulation phase-locked to ACC theta (Figure S3E), again excluding the possibility of a simple time-dependent change. Notably, when we limited the analysis to the phase-locked pairs with top 50 or 20 percent of co-firing index in each the session, the increase during the remote session was even more robust (Figure S6I), raising the possibility that only a subpopulation of CA1 neurons are involved in these changes. Furthermore, mice with higher co-firing of distal CA1 neuron pairs also demonstrated larger ACC-CA1 theta and fast-gamma instantaneous amplitude correlations, as well as increased

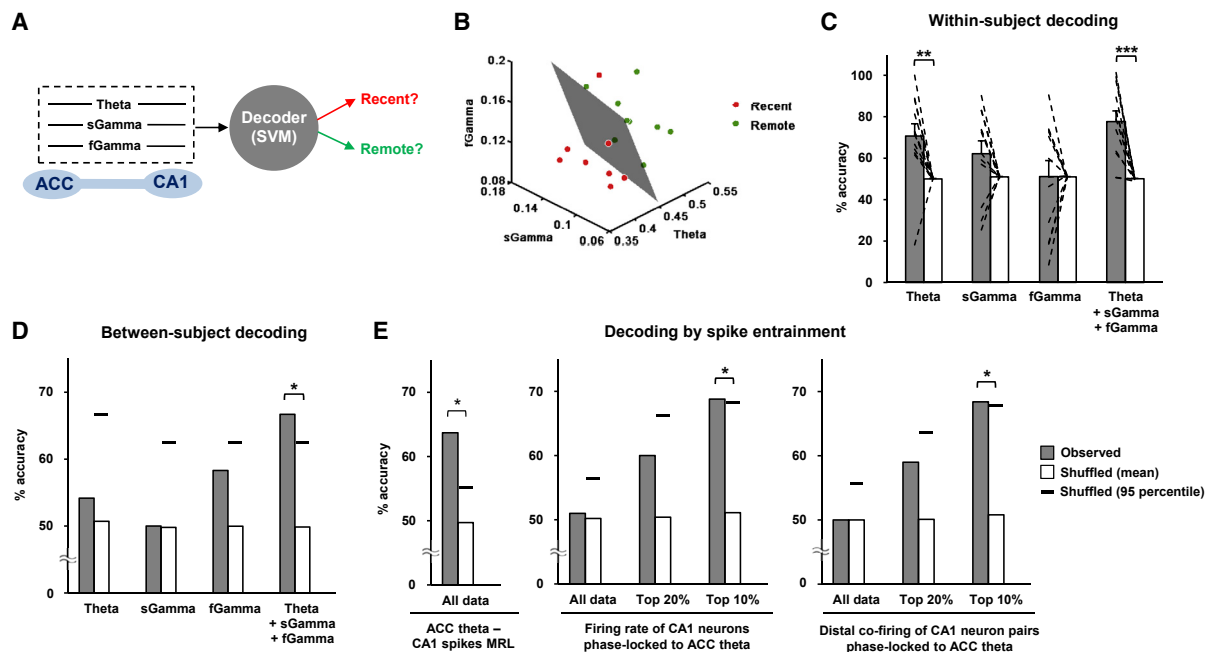


Figure 6. ACC-CA1 Synchronization Pattern Can Accurately Decode the Age of Fear Memory

(A) ACC-CA1 instantaneous amplitude correlation values at theta, slow-gamma (sGamma), and fast-gamma (fGamma) frequencies from part of the data during non-freezing periods were used to generate the decoder using a support vector machine (SVM). The rest of the data were tested by the decoder to determine whether they were from the recent or remote session.

(B) A representative discriminating plane which classifies multi-frequency correlation data into recent and remote sessions.

(C) For each mouse, decoding accuracy (observed) was calculated by classifying each non-freezing epoch into either recent or remote, using a decoder generated by the other epochs. As a control, accuracy (shuffled) was calculated using decoders generated by data with class labels (recent/remote) randomly shuffled. Accuracy values were averaged over all mice, and significant differences from shuffled controls are indicated by asterisks (theta: $t_{11} = 3.51$, $p = 0.005$; sGamma: $t_{11} = 1.78$, $p = 0.102$; fGamma: $t_{11} = 0.02$, $p = 0.986$; theta + sGamma + fGamma: $t_{11} = 5.45$, $p < 0.001$; $n = 12$ mice, two-tailed within-subject t test).

(D) Decoding accuracy (observed) was calculated by classifying each mouse into either recent or remote, using a decoder generated by the other mice. Shuffled control was performed as for within-subject decoding, and the 95th percentile of its accuracy values is shown by bars. Significant differences from shuffled controls are indicated by asterisks (theta, sGamma, and fGamma: $p > 0.05$; theta + sGamma + fGamma: $p < 0.05$; $n = 12$ mice, permutation test; see STAR Methods).

(E) Decoding accuracy was calculated by classifying each CA1 neuron (left, middle) or neuron pair (right) as either recorded at the recent or remote session, using a decoder generated by the other neurons or neuron pairs. Phase-locking strength (MRL) of CA1 neurons to ACC theta (left; $n = 110$ [recent] and 91 [remote] neurons), firing rate of CA1 neurons phase-locked to ACC theta (middle; $n = 77$ [recent] and 76 [remote] neurons), and co-firing index of CA1 neuron pairs that are both phase-locked to ACC theta (right; $n = 74$ [recent] and 120 [remote] neuron pairs), all during non-freezing periods, were used to generate the decoder. Shuffled control was performed as in (D), and the 95th percentile of its accuracy values is shown by bars. Significant differences from shuffled controls are indicated by asterisks ($p < 0.05$, permutation test).

For all bar graphs, data are represented as mean \pm SEM, and dotted lines indicate values from individual mice. * $p < 0.05$, ** $p < 0.01$, and *** $p < 0.001$.

freezing levels during remote recall (Figures 4D and 4E), linking ACC entrainment of long-distance CA1 co-firing to successful recall.

Sequential ACC-CA1 Interactions Predict Remote Memory Recall

To understand how the communication between ACC and CA1 changes dynamically on a timescale relevant to memory recall, we analyzed the ACC-CA1 interaction specifically at freezing onset and offset. Although the increased theta correlation during the remote session was seen uniformly across non-freezing periods (Figure 5A), the increased fast-gamma correlation was observed specifically at 1–2 s before freezing onset (Figure 5B). Concomitantly, CA1 distal neuron pairs phase-locked to ACC theta exhibited a gradual increase of co-firing prior to freezing onset only during the remote session and then remained persis-

tently high into the freezing period (Figure 5C). These results indicate that distinct types of ACC-CA1 interactions occur sequentially prior to freezing onset (Figure 5D), suggesting that the recall of remote fear memory may be a dynamic multi-stage process.

Memory Age Can Be Decoded by the Patterns of ACC-CA1 Synchrony

We found that ACC-CA1 interaction is augmented at multiple frequencies during remote memory recall, entraining CA1 long-distance neuronal synchrony. We next wondered if the increase of ACC-CA1 interaction from recent to remote memory is robust enough, both within and between individual mice, to be used as an index of the age of the memory. To test this, we used a support vector machine (SVM) algorithm (see STAR Methods for details) to generate a classifier that could discriminate the age of

the memory being recalled on the basis of various patterns of the ACC-CA1 interaction (Figure 6A).

First, we tried to decode memory age during a single non-freezing period on the basis of the ACC-CA1 LFP instantaneous amplitude correlation pattern (Figure 6B), using a classifier generated with the remaining data from the same mouse (within-subject decoding; similar “leave-one-out” approaches have been used in previous studies (Ecker et al., 2010; Kamitani and Tong, 2005)). Decoding accuracy was significantly higher than shuffled controls (see STAR Methods for details) when ACC-CA1 theta correlation, but not slow-gamma or fast-gamma correlation, was used as input (Figure 6C). Increasing the dimensionality by using correlations at all three frequencies as input resulted in increased accuracy, well above the shuffled controls (Figure 6C).

Next, we attempted to decode whether a mouse was recalling a recent or remote memory over an entire 10 min session on the basis of the ACC-CA1 correlation pattern, using a classifier trained on data from the rest of mice (between-subject decoding). Decoding accuracy was again significantly higher than the shuffled control when correlation information at all frequencies was used (Figure 6D), demonstrating that multi-frequency correlation pattern is robust enough for successful cross-individual decoding.

Last, we tried to decode the memory age on the basis of the entrainment of CA1 spike activity by ACC. Using the classifier trained on phase-locking strength of CA1 neurons to ACC theta, we were able to decode whether neurons were recorded during the recent session or remote session (Figure 6E, left). Interestingly, while firing rate and co-firing of CA1 neurons phase-locked to ACC theta showed chance-level decoding accuracy when the entire population of CA1 neurons was used as an input, the accuracy became significantly higher than the shuffled control data when only the neurons or neuronal pairs with top 10 percent of these values for each session were used (Figure 6E, middle and right). These results may indicate that only a subpopulation of CA1 neurons codes the age of memory, consistent with the idea of sparse coding of remote memory by CA1 neurons.

DISCUSSION

Although distinct contributions of CA1 and the ACC to recent and remote memory have been well studied (Bontempi et al., 1999; Frankland and Bontempi, 2005; Frankland et al., 2004; Maviel et al., 2004; Squire, 1992), previous physiological experiments have primarily focused on interactions during systems consolidation (Khodagholy et al., 2017; Xia et al., 2017). Here we examined how dynamic ACC-CA1 interactions during recall evolve across time at both the population and single-cell levels. During remote recall, population activity at theta and fast-gamma frequencies became more synchronized between ACC and CA1 during non-freezing periods, suggesting that these regions cooperate during exposure to the contextual cues to facilitate memory recall. In addition, ACC exhibited enhanced entrainment of CA1 neuronal activity, generating synchronous firing among distally located neurons. Finally, we found that the changes in ACC-CA1 synchrony from recent to remote memory are robust enough to use as a tool to decode the age of memory.

The multiple trace theory posits that the hippocampus is always involved in the storage and retrieval of detailed episodic information of a memory, while schematic information of the same memory is established in the cortex (Moscovitch et al., 2016; Winocur and Moscovitch, 2011; Winocur et al., 2010). Consistent with this, we find that both the ACC and CA1 are engaged during remote memory retrieval in a coordinated manner. Although we did not examine the specific information content in the respective regions, it is possible that a schematic representation of the fear-associated context in ACC and contextual details of the environment in CA1 are integrated to facilitate a complete recall of contextual memory (Moscovitch et al., 2016; Winocur and Moscovitch, 2011). This notion is supported by our findings that ACC-CA1 cross-regional interaction, but not region-autonomous ACC activity, is enhanced during the remote session (Figures 2D, 3C, 3D, and S1B). Consistent with this, a recent study has found that non-aversive contextual re-exposure at the remote time point enhances ACC-CA1 cross-regional interaction (Wirt and Hyman, 2019), suggesting that the recruitment of ACC-CA1 pathway at remote recall may be a general mechanism common to multiple forms of memory. Furthermore, although we cannot exclude the possibility that non-freezing periods engage cognitive processes in addition to recall, such as updating, extinction, and reconsolidation, we did observe a strong correlation between ACC-entrained CA1 synchronous firing during these periods and freezing levels (Figures 4D and 4E), suggesting an active role in recall.

Notably, we have observed a dynamic temporal sequence of distinct types of ACC-CA1 interactions at the onset of freezing (Figure 5), consistent with their role in recall. This sequence starts with the increase of theta amplitude correlation between ACC and CA1 upon exposure to contextual cues through exploration, followed by a rise of ACC-CA1 fast-gamma correlation, possibly initiating the recall process. This is followed by increased co-firing of distal CA1 neuron pairs entrained to ACC theta, potentially sustaining the ongoing recall during freezing. This sequential model is consistent with human event-related potential studies showing that memory retrieval involves different phases of activity spread over time and brain region, including the frontal and temporal cortices (Allan et al., 1998; Mecklinger, 2000; Rugg and Curran, 2007), and supports multi-process models of memory retrieval (Jacoby, 1991; Mandler, 1980). Combined with a recent study showing that human temporal cortex and medial temporal lobe exhibit synchronous activity immediately before successful recall of memory (Vaz et al., 2019), our findings suggest that the cortical-hippocampal interaction during the pre-recall period might be a conserved phenomenon that could facilitate subsequent memory retrieval.

It remains to be answered which pathways between ACC and CA1 would mediate these activity changes. Although a direct connection from ACC to CA1 has recently been reported (Rajasekharan et al., 2015), there are extensive indirect connections from ACC to CA1 via multiple brain regions, including the nucleus reuniens of the thalamus (Vertes, 2002; Vertes et al., 2007) and entorhinal/perirhinal cortices (Jones and Witter, 2007; Witter et al., 2000). In particular, the nucleus reuniens has recently been shown to mediate behavioral task-specific activity between the prefrontal cortex and hippocampus (Hallock

et al., 2016; Ito et al., 2015, 2018), suggesting that the ACC-reuniens-CA1 pathway might subserve top-down theta entrainment underlying remote memory recall. The stronger influence of ACC theta on CA1 fast-gamma, either via direct or indirect pathways, could allow ACC to better co-modulate fast-gamma in both CA1 and ACC, resulting in the enhanced fast-gamma synchrony between these regions. Consistent with previous work demonstrating the role of fast-gamma coupling between CA1 and the entorhinal cortex in spatial processing (Yamamoto et al., 2014), our data suggest that fast-gamma synchrony between ACC and CA1 may coordinate the recall of a consolidated contextual memory.

On the single-unit level, we observed that neuronal pairs in CA1 that are distally, but not proximally, located increased their co-firing during remote recall. Furthermore, this property was significantly enhanced in pairs coupled to the ACC theta oscillation, implying a cross-regional remodeling of functional connectivity to support top-down recall of remote memory. Synchronous neuronal activity in the hippocampus has previously been implicated in memory formation and retrieval (Cheng and Frank, 2008; Rajasethupathy et al., 2015). Although differential synchronous activities between proximal and distal neuronal pairs have rarely been reported, previous studies have suggested that CA1 neurons are functionally clustered at 200–400 μm alternating segments (Hampson et al., 1999; Yang et al., 2014). One possibility is that remote memory representation may be embedded in spatially distant alternating segments, which induces long-distance synchronous activity when recalled. In line with both the suggestion that CA1 contains a highly efficient and sparse memory trace at remote time points (Goshen et al., 2011) and our observations that only a fraction of CA1 neurons exhibit time-dependent changes (Figures 6E and S6I), the enhancement of non-local circuit synchrony may enable fewer, sparsely distributed neurons to maintain memory, increasing efficiency and preserving memory capacity.

In contrast to remote recall, ACC-CA1 interactions during recent memory recall were very similar to those observed during the pre-acquisition baseline session. This is in contrast to the enhanced cross-regional interactions between hippocampus and amygdala observed during recent recall (Seidenbecher et al., 2003; Xu et al., 2016). Indeed, we also observed an enhanced instantaneous amplitude correlation between CA1 and BLA at theta frequency during both recent and remote memory recall (Figure S6J). Thus, although recent memory is mediated primarily by enhanced CA1-BLA interactions, remote memory involves the additional recruitment of the ACC-CA1 circuit. Although we did not examine the detailed time course of this transition, previous studies have shown almost identical patterns of physiological and behavioral changes involved in remote memory formation at any point after ~ 15 days of conditioning in mice (Frankland et al., 2004; Kitamura et al., 2017), suggesting that the recruitment of the ACC-CA1 interaction may be established within the first two weeks of memory acquisition.

Finally, we demonstrated that the signature of ACC-CA1 interactions during recent and remote recall is reliable and consistent across individual mice, such that both the LFP instantaneous amplitude correlation at different frequencies and cross-regional entrainment of neuronal activity were suffi-

cient to accurately discriminate recent from remote recall using a SVM classifier. The ability to accurately determine memory age on the basis of oscillation data alone suggests that this approach may be translatable to humans. Furthermore, decoding was successful in a between-subject manner, which has been difficult to achieve in the decoding of behavioral and cognitive states. The ability of between-subject decoding raises the possibility that with a sufficient amount of training data, no prior knowledge of an individual's recall-related EEG pattern would be necessary for memory age determination.

This study adds to the extensive literature supporting an active role of the prefrontal cortex and hippocampus in the recall of remote memory. Our data suggest that memory consolidation alters the physiological interactions between these regions in a robust and stereotypical manner, providing a novel biomarker for both laboratory and clinical studies examining memory impairments in age and disease.

STAR★METHODS

Detailed methods are provided in the online version of this paper and include the following:

- KEY RESOURCES TABLE
- LEAD CONTACT AND MATERIALS AVAILABILITY
- EXPERIMENTAL MODEL AND SUBJECT DETAILS
- METHOD DETAILS
 - Contextual fear conditioning apparatus
 - Microdrive construction
 - Surgery
 - Experimental procedure
 - Histology
 - Data acquisition
- QUANTIFICATION AND STATISTICAL ANALYSIS
 - Behavioral analysis
 - Unit isolation and classification
 - LFP power analysis
 - LFP-LFP instantaneous amplitude correlation analysis
 - LFP-LFP phase difference analysis
 - LFP-LFP Granger causality analysis
 - LFP-LFP cross-frequency coupling analysis
 - LFP-spike phase-locking analysis
 - Co-firing analysis
 - Place cell analysis
 - Ripple detection
 - Support vector machine (SVM) analysis
 - Statistics
- DATA AND CODE AVAILABILITY

SUPPLEMENTAL INFORMATION

Supplemental Information can be found online at <https://doi.org/10.1016/j.celrep.2019.11.075>.

ACKNOWLEDGMENTS

We thank K.Z. Tanaka for critical reading of the manuscript, K. Niisato for instruction on microdrive assembly, and all the other members of the Laboratory

for Circuit and Behavioral Physiology (McHugh lab) for their support. We thank the RIKEN Advanced Manufacturing Team for their assistance in microdrive production. This work was supported by RIKEN BSI and CBS (T.J.M.); Japan Society for the Promotion of Science (JSPS) Kakenhi grants 19H05646 (T.J.M.) and 24700346 (Y.M.); and the RIKEN Special Postdoctoral Researcher Program (Y.M.).

AUTHOR CONTRIBUTIONS

Y.M. and T.J.M. conceived the study and designed the experiments. Y.M. performed the experiments and analyzed data. F.B. and A.B. assisted in the application of DeepLabCut analysis of behavioral data. D.P. provided technical assistance. Y.M. and T.J.M. wrote the manuscript with input from all authors.

DECLARATION OF INTERESTS

The authors declare no competing interests.

Received: March 14, 2019

Revised: November 3, 2019

Accepted: November 18, 2019

Published: December 17, 2019

SUPPORTING CITATIONS

The following references appear in the Supplemental Information: Schmitzer-Torbert et al., 2005.

REFERENCES

- Adhikari, A., Sigurdsson, T., Topiwala, M.A., and Gordon, J.A. (2010). Cross-correlation of instantaneous amplitudes of field potential oscillations: a straightforward method to estimate the directionality and lag between brain areas. *J. Neurosci. Methods* *191*, 191–200.
- Allan, K., Wilding, E.L., and Rugg, M.D. (1998). Electrophysiological evidence for dissociable processes contributing to recollection. *Acta Psychol. (Amst.)* *98*, 231–252.
- Bair, W., Zohary, E., and Newsome, W.T. (2001). Correlated firing in macaque visual area MT: time scales and relationship to behavior. *J. Neurosci.* *21*, 1676–1697.
- Barnett, L., and Seth, A.K. (2014). The MVGC multivariate Granger causality toolbox: a new approach to Granger-causal inference. *J. Neurosci. Methods* *223*, 50–68.
- Boehringer, R., Polygalov, D., Huang, A.J.Y., Middleton, S.J., Robert, V., Wintzer, M.E., Piskowski, R.A., Chevaleyre, V., and McHugh, T.J. (2017). Chronic loss of CA2 transmission leads to hippocampal hyperexcitability. *Neuron* *94*, 642–655.e9.
- Bontempi, B., Laurent-Demir, C., Destrade, C., and Jaffard, R. (1999). Time-dependent reorganization of brain circuitry underlying long-term memory storage. *Nature* *400*, 671–675.
- Buzsáki, G. (2004). Large-scale recording of neuronal ensembles. *Nat. Neurosci.* *7*, 446–451.
- Buzsáki, G. (2015). Hippocampal sharp wave-ripple: a cognitive biomarker for episodic memory and planning. *Hippocampus* *25*, 1073–1188.
- Buzsáki, G., and Wang, X.J. (2012). Mechanisms of gamma oscillations. *Annu. Rev. Neurosci.* *35*, 203–225.
- Cheng, S., and Frank, L.M. (2008). New experiences enhance coordinated neural activity in the hippocampus. *Neuron* *57*, 303–313.
- Colgin, L.L., Denninger, T., Fyhn, M., Hafting, T., Bonnevie, T., Jensen, O., Moser, M.B., and Moser, E.I. (2009). Frequency of gamma oscillations routes flow of information in the hippocampus. *Nature* *462*, 353–357.
- Courtin, J., Chaudun, F., Rozeske, R.R., Karalis, N., Gonzalez-Campo, C., Wurtz, H., Abdi, A., Baufreton, J., Bienvenu, T.C., and Herry, C. (2014). Prefrontal parvalbumin interneurons shape neuronal activity to drive fear expression. *Nature* *505*, 92–96.
- Ecker, C., Marquand, A., Mourão-Miranda, J., Johnston, P., Daly, E.M., Brammer, M.J., Maltezos, S., Murphy, C.M., Robertson, D., Williams, S.C., and Murphy, D.G. (2010). Describing the brain in autism in five dimensions—magnetic resonance imaging-assisted diagnosis of autism spectrum disorder using a multiparameter classification approach. *J. Neurosci.* *30*, 10612–10623.
- Eichenbaum, H. (2017). Prefrontal-hippocampal interactions in episodic memory. *Nat. Rev. Neurosci.* *18*, 547–558.
- Frankland, P.W., and Bontempi, B. (2005). The organization of recent and remote memories. *Nat. Rev. Neurosci.* *6*, 119–130.
- Frankland, P.W., Bontempi, B., Talton, L.E., Kaczmarek, L., and Silva, A.J. (2004). The involvement of the anterior cingulate cortex in remote contextual fear memory. *Science* *304*, 881–883.
- Goshen, I., Brodsky, M., Prakash, R., Wallace, J., Gradinaru, V., Ramakrishnan, C., and Deisseroth, K. (2011). Dynamics of retrieval strategies for remote memories. *Cell* *147*, 678–689.
- Hallock, H.L., Wang, A., and Griffin, A.L. (2016). Ventral midline thalamus is critical for hippocampal-prefrontal synchrony and spatial working memory. *J. Neurosci.* *36*, 8372–8389.
- Hampson, R.E., Simeral, J.D., and Deadwyler, S.A. (1999). Distribution of spatial and nonspatial information in dorsal hippocampus. *Nature* *402*, 610–614.
- Hung, C.P., Kreiman, G., Poggio, T., and DiCarlo, J.J. (2005). Fast readout of object identity from macaque inferior temporal cortex. *Science* *310*, 863–866.
- Ito, H.T., Zhang, S.J., Witter, M.P., Moser, E.I., and Moser, M.B. (2015). A prefrontal-thalamo-hippocampal circuit for goal-directed spatial navigation. *Nature* *522*, 50–55.
- Ito, H.T., Moser, E.I., and Moser, M.B. (2018). Supramammillary nucleus modulates spike-time coordination in the prefrontal-thalamo-hippocampal circuit during navigation. *Neuron* *99*, 576–587.e5.
- Jacoby, L.L. (1991). A process dissociation framework: separating automatic from intentional uses of memory. *J. Mem. Lang.* *30*, 513–541.
- Jones, B.F., and Witter, M.P. (2007). Cingulate cortex projections to the parahippocampal region and hippocampal formation in the rat. *Hippocampus* *17*, 957–976.
- Kamitani, Y., and Tong, F. (2005). Decoding the visual and subjective contents of the human brain. *Nat. Neurosci.* *8*, 679–685.
- Khodagholy, D., Gelinás, J.N., and Buzsáki, G. (2017). Learning-enhanced coupling between ripple oscillations in association cortices and hippocampus. *Science* *358*, 369–372.
- Kitamura, T., Ogawa, S.K., Roy, D.S., Okuyama, T., Morrissey, M.D., Smith, L.M., Redondo, R.L., and Tonegawa, S. (2017). Engrams and circuits crucial for systems consolidation of a memory. *Science* *356*, 73–78.
- Likhtik, E., Stujenske, J.M., Topiwala, M.A., Harris, A.Z., and Gordon, J.A. (2014). Prefrontal entrainment of amygdala activity signals safety in learned fear and innate anxiety. *Nat. Neurosci.* *17*, 106–113.
- Livneh, U., and Paz, R. (2012). Amygdala-prefrontal synchronization underlies resistance to extinction of aversive memories. *Neuron* *75*, 133–142.
- Mandler, G. (1980). Recognizing: the judgment of previous occurrence. *Psychol. Rev.* *87*, 252–271.
- Mathis, A., Mamidanna, P., Cury, K.M., Abe, T., Murthy, V.N., Mathis, M.W., and Bethge, M. (2018). DeepLabCut: markerless pose estimation of user-defined body parts with deep learning. *Nat. Neurosci.* *21*, 1281–1289.
- Maviel, T., Durkin, T.P., Menzaghi, F., and Bontempi, B. (2004). Sites of neocortical reorganization critical for remote spatial memory. *Science* *305*, 96–99.
- Mecklinger, A. (2000). Interfacing mind and brain: a neurocognitive model of recognition memory. *Psychophysiology* *37*, 565–582.
- Middleton, S.J., and McHugh, T.J. (2016). Silencing CA3 disrupts temporal coding in the CA1 ensemble. *Nat. Neurosci.* *19*, 945–951.

- Middleton, S.J., Kneller, E.M., Chen, S., Ogiwara, I., Montal, M., Yamakawa, K., and McHugh, T.J. (2018). Altered hippocampal replay is associated with memory impairment in mice heterozygous for the *Scn2a* gene. *Nat. Neurosci.* *21*, 996–1003.
- Moscovitch, M., Cabeza, R., Winocur, G., and Nadel, L. (2016). Episodic memory and beyond: the hippocampus and neocortex in transformation. *Annu. Rev. Psychol.* *67*, 105–134.
- Place, R., Farovik, A., Brockmann, M., and Eichenbaum, H. (2016). Bidirectional prefrontal-hippocampal interactions support context-guided memory. *Nat. Neurosci.* *19*, 992–994.
- Quirk, M.C., and Wilson, M.A. (1999). Interaction between spike waveform classification and temporal sequence detection. *J. Neurosci. Methods* *94*, 41–52.
- Rajasethupathy, P., Sankaran, S., Marshel, J.H., Kim, C.K., Ferenczi, E., Lee, S.Y., Berndt, A., Ramakrishnan, C., Jaffe, A., Lo, M., et al. (2015). Projections from neocortex mediate top-down control of memory retrieval. *Nature* *526*, 653–659.
- Remondes, M., and Wilson, M.A. (2013). Cingulate-hippocampus coherence and trajectory coding in a sequential choice task. *Neuron* *80*, 1277–1289.
- Rosenbaum, R.S., Priselac, S., Köhler, S., Black, S.E., Gao, F., Nadel, L., and Moscovitch, M. (2000). Remote spatial memory in an amnesic person with extensive bilateral hippocampal lesions. *Nat. Neurosci.* *3*, 1044–1048.
- Rugg, M.D., and Curran, T. (2007). Event-related potentials and recognition memory. *Trends Cogn. Sci.* *11*, 251–257.
- Schmitzer-Torbert, N., Jackson, J., Henze, D., Harris, K., and Redish, A.D. (2005). Quantitative measures of cluster quality for use in extracellular recordings. *Neuroscience* *137*, 1–11.
- Scoville, W.B., and Milner, B. (1957). Loss of recent memory after bilateral hippocampal lesions. *J. Neurol. Neurosurg. Psychiatry* *20*, 11–21.
- Seidenbecher, T., Laxmi, T.R., Stork, O., and Pape, H.C. (2003). Amygdalar and hippocampal theta rhythm synchronization during fear memory retrieval. *Science* *301*, 846–850.
- Siapas, A.G., Lubenov, E.V., and Wilson, M.A. (2005). Prefrontal phase locking to hippocampal theta oscillations. *Neuron* *46*, 141–151.
- Sigurdsson, T., Stark, K.L., Karayiorgou, M., Gogos, J.A., and Gordon, J.A. (2010). Impaired hippocampal-prefrontal synchrony in a genetic mouse model of schizophrenia. *Nature* *464*, 763–767.
- Skaggs, W.E., McNaughton, B.L., Gothard, K.M., and Markus, E.J. (1993). An information-theoretic approach to deciphering the hippocampal code. In *Advances in Neural Information Processing Systems 5 (NIPS 1992)*, S.J. Hanson, J.D. Cowan, and C.L. Giles, eds. (Morgan Kaufmann), pp. 1030–1037.
- Squire, L.R. (1992). Memory and the hippocampus: a synthesis from findings with rats, monkeys, and humans. *Psychol. Rev.* *99*, 195–231.
- Squire, L.R., and Alvarez, P. (1995). Retrograde amnesia and memory consolidation: a neurobiological perspective. *Curr. Opin. Neurobiol.* *5*, 169–177.
- Tamura, M., Spellman, T.J., Rosen, A.M., Gogos, J.A., and Gordon, J.A. (2017). Hippocampal-prefrontal theta-gamma coupling during performance of a spatial working memory task. *Nat. Commun.* *8*, 2182.
- Tanaka, K.Z., He, H., Tomar, A., Niisato, K., Huang, A.J.Y., and McHugh, T.J. (2018). The hippocampal engram maps experience but not place. *Science* *361*, 392–397.
- Tort, A.B., Komorowski, R., Eichenbaum, H., and Kopell, N. (2010). Measuring phase-amplitude coupling between neuronal oscillations of different frequencies. *J. Neurophysiol.* *104*, 1195–1210.
- Vaz, A.P., Inati, S.K., Brunel, N., and Zaghoul, K.A. (2019). Coupled ripple oscillations between the medial temporal lobe and neocortex retrieve human memory. *Science* *363*, 975–978.
- Vertes, R.P. (2002). Analysis of projections from the medial prefrontal cortex to the thalamus in the rat, with emphasis on nucleus reuniens. *J. Comp. Neurol.* *442*, 163–187.
- Vertes, R.P., Hoover, W.B., Szigeti-Buck, K., and Leranath, C. (2007). Nucleus reuniens of the midline thalamus: link between the medial prefrontal cortex and the hippocampus. *Brain Res. Bull.* *71*, 601–609.
- Winocur, G., and Moscovitch, M. (2011). Memory transformation and systems consolidation. *J. Int. Neuropsychol. Soc.* *17*, 766–780.
- Winocur, G., Moscovitch, M., and Bontempi, B. (2010). Memory formation and long-term retention in humans and animals: convergence towards a transformation account of hippocampal-neocortical interactions. *Neuropsychologia* *48*, 2339–2356.
- Wirt, R.A., and Hyman, J.M. (2019). ACC theta improves hippocampal contextual processing during remote recall. *Cell. Rep.* *27*, 2313–2327.e4.
- Witter, M.P., Wouterlood, F.G., Naber, P.A., and Van Haeften, T. (2000). Anatomical organization of the parahippocampal-hippocampal network. *Ann. N Y Acad. Sci.* *911*, 1–24.
- Xia, F., Richards, B.A., Tran, M.M., Josselyn, S.A., Takehara-Nishiuchi, K., and Frankland, P.W. (2017). Parvalbumin-positive interneurons mediate neocortical-hippocampal interactions that are necessary for memory consolidation. *eLife* *6*, e27868.
- Xu, C., Krabbe, S., Grundemann, J., Botta, P., Fadok, J.P., Osakada, F., Saur, D., Grewe, B.F., Schnitzer, M.J., Callaway, E.M., et al. (2016). Distinct hippocampal pathways mediate dissociable roles of context in memory retrieval. *Cell* *167*, 961–972.e16.
- Yamamoto, J., Suh, J., Takeuchi, D., and Tonegawa, S. (2014). Successful execution of working memory linked to synchronized high-frequency gamma oscillations. *Cell* *157*, 845–857.
- Yang, S., Yang, S., Moreira, T., Hoffman, G., Carlson, G.C., Bender, K.J., Alger, B.E., and Tang, C.M. (2014). Interlamellar CA1 network in the hippocampus. *Proc. Natl. Acad. Sci. U S A* *111*, 12919–12924.

STAR★METHODS

KEY RESOURCES TABLE

REAGENT or RESOURCE	SOURCE	IDENTIFIER
Experimental Models: Organisms/Strains		
Mouse: C57BL6/J	Bred in-house	RRID: IMSR_JAX:000664
Software and Algorithms		
MATLAB R2013a	MathWorks	RRID: SCR_001622
SpikeSort 3D v2.5.1.0	Neuralynx	RRID: SCR_014478
Cheetah v5.6.0	Neuralynx	https://neuralynx.com/
FreezeFrame v2.28	Actimetrics	RRID: SCR_014429
IBM SPSS v21	IBM	RRID: SCR_002865
CircStat: A MATLAB Toolbox for Circular Statistics	P. Berens	RRID: SCR_016651

LEAD CONTACT AND MATERIALS AVAILABILITY

This study did not generate new unique reagents. Further information should be directed to the Lead Contact, Thomas J. McHugh (thomas.mchugh@riken.jp).

EXPERIMENTAL MODEL AND SUBJECT DETAILS

Adult male wild-type C57BL/6J mice, bred in-house, were used for all experiments. Mice were in the range of 3-7 months old over the course of the experiments. Mice were maintained on a 12-h light/dark cycle and provided with food and water *ad libitum*. All experiments were performed at the light phase. All procedures were approved by the RIKEN Institutional Animal Care and Use Committee and complied with all relevant ethical regulations.

METHOD DETAILS

Contextual fear conditioning apparatus

Baseline, training and recall sessions of contextual fear conditioning (CFC) were all conducted in a brightly lit behavioral training room. The chamber, consisting of an acrylic plastic front and back with aluminum walls on each side, measured 30 × 25 × 21 cm (Med Associates ENV-008, Georgia, VT). The floor of the chamber consisted of 36 stainless steel rods of 3.2 mm diameter and spaced 7.9 mm apart and was connected via a cable harness to a shock generator. The chamber was cleaned between animals with 70% ethanol, and a solution of 1% acetic acid was placed beneath the chamber during the experiment to provide an olfactory cue. Freezing behavior was video recorded by the camera located behind the chamber at a frame rate of 3.75 Hz. Shock deliveries and video recordings were controlled by FreezeFrame software (Actimetrics, Wilmette, IL).

Microdrive construction

Custom microdrives were manufactured with the assistance of the Advanced Manufacturing Team at RIKEN. The microdrive was constructed on a 3D-printed plastic base which held an interface board (EIB-36; Neuralynx, Bozeman, MT) and ten nichrome (14 μm diameter) tetrodes, all of which were independently adjustable along the z axis. These ten tetrodes were positioned so that three were targeted to the right ACC (center coordinate is X +0.8, Y +0.3, Z -1.6), two to right dorsal CA1 (X -2.0, Y +1.5, Z -1.3), three to the right BLA (X -2.0, Y +3.3, Z -4.3), and two to the right ventral hippocampal commissure (vHC; X -0.8, Y +0.7, Z -2.4) where the reference signal was recorded. All tetrodes were gold plated to a resistance of 200–300 kΩ prior to surgery.

Surgery

Mice were anesthetized using Avertin (2, 2, 2-tribromoethanol; Sigma-Aldrich, 476 mg/kg, i.p) and placed into a stereotaxic frame (Kopf). The skull was leveled using bregma and lambda landmarks. Small craniotomies were made individually over ACC (X +0.8, Y +0.3, Z -1.6), CA1 (X -2.0, Y +1.5, Z -1.3), BLA (X -2.0, Y +3.3, Z -4.3) and vHC (X -0.8, Y +0.7, Z -2.4). Tetrodes were then inserted to their respective target regions simultaneously, ensuring that all tetrodes were targeted to the stereotaxic coordinates described

above. In addition, a stainless steel screw was implanted above the left cerebellum to serve as a ground. The microdrive was fixed to the skull with dental cement (Super-Bond C&B, Sun Medical). Following recovery from anesthesia, mice were returned to their home cage where they were housed individually.

After surgery, tetrodes in CA1 were slightly adjusted into the pyramidal cell layer, which was identified by numerous large amplitude pyramidal cell spikes and sharp-wave ripples during periods of immobility. Tetrodes in ACC and BLA were adjusted only minimally ($\sim \pm 100 \mu\text{m}$) to obtain maximal unit detection. Tetrodes in the vHC were left unadjusted.

Experimental procedure

Once stable unit detection was obtained in all regions, which typically took 2–3 weeks post-surgery, the contextual fear conditioning experiment was conducted. On Day 1, LFP and spike activity were recorded as the mice were placed in a small square enclosure (habituation box). Tetrodes were occasionally minimally adjusted to ensure their placement in the pyramidal layer (for CA1) and reasonable unit detection (for ACC/BLA) and at least 1 hour was allowed before subsequent procedures. Neural activity was then recorded in the habituation box for 10 min (habituation session). After resting in the animal housing room for 30 min, mice were placed in the CFC chamber for 10 min and their activity was recorded (baseline session). After 30 min of rest in the housing room they were again brought back to the CFC chamber and fear-conditioned with a 2" 0.5 mA foot shock delivered three times at 1 min intervals.

On Day 2, mice were first brought to the habituation box at the same time of the day as Day 1 and LFP and spike activity was recorded for 10 minutes. After 30 min of rest in the housing room they were brought to the CFC chamber and their recall of contextual fear memory was assessed for 10 min while neural activity was recorded (recent session). On Day 26–28 the protocol used on Day 2 was repeated and fear recall was assessed again (remote session).

Histology

At the conclusion of the experiment mice underwent terminal anesthesia and tetrode positions were marked by electrolytic lesioning of brain tissue (30 μA current for 7 s through each electrode individually). Brains were fixed with cardiac perfusion of 4% paraformaldehyde (PFA) followed by post-fix in PFA for 24 hours and coronal slices with 50 μm thickness were prepared on a cryostat. Tetrode placement was confirmed by standard light microscopy.

Data acquisition

Recordings were obtained via a unity gain headstage preamplifier (HS-36; Neuralynx) connected to a flexible tether cable (TETH-HS-36-Flex-EXT; Neuralynx) suspended from the ceiling with a rubber band, which allowed mice to freely move their head up and down with minimal force. Data were acquired using a 32-channel Digital Lynx 4SX acquisition system with Cheetah software (Neuralynx). Signals were sampled at 32,000 Hz and filtered between 1–9,000 Hz for LFP and 600–6,000 Hz for spikes. Only the spikes exceeding a threshold of 50 μV were recorded. After recordings, LFP was down-sampled to 1,600 Hz for subsequent analyses.

QUANTIFICATION AND STATISTICAL ANALYSIS

Behavioral analysis

Non-freezing and freezing periods were determined by manually examining all video frames over the entire recording. The periods of each state lasting shorter than 1.28 s were excluded from analysis.

For some analyses, more detailed behavioral categorization was performed by tracking each body point of the mice using the DeepLabCut algorithm (Mathis et al., 2018). The tilt in the view-angle was first corrected to provide a top-down view of the chamber, which was achieved via an affine transformation of every frame using `cproject` and `fitgeotrans` functions of MATLAB (Figure S4A). The mouse snout, abdomen, tail base and headstage were tracked using a segmentation algorithm based on a deep convolutional network. The tracking reliability was provided as a likelihood measure by DeepLabCut, and frames with < 60% reliability were excluded. The XY positional information was converted into velocities (cm/s) and instantaneous values were smoothed with a moving average across 3 consecutive frames, which were then used to classify behavior. Exploration was defined as the period with > 4 cm/s snout, > 6 cm/s abdomen and > 8 cm/s tail base. Head movement was defined as the period with > 4 cm/s snout, ≤ 6 cm/s abdomen and ≤ 8 cm/s tail base. Freezing was defined as the period with ≤ 4 cm/s snout. The periods of each state lasting shorter than 1.28 s were excluded from analysis. The classification for freezing periods was verified to match the manual classification above 80% for all sessions/mice (Figure S4C). The classification for exploration and head movement periods was also verified by human expert. Small changes in threshold values for velocity did not significantly affect the results.

Mouse tracking with a higher temporal precision was performed based on the location of LEDs on mouse head which was recorded from the top of the CFC chamber at 30 Hz. Trajectories of the mice were corrected by removing artifacts caused by transient tracking errors and were smoothed with a Gaussian kernel of 0.05 SD width.

Unit isolation and classification

Spike sorting was performed using SpikeSort3D software (Neuralynx), with putative cells clustered manually in three-dimensional projections of spike amplitudes from individual electrodes of a tetrode. Putative interneurons ($\sim 5\%$ for CA1 and $\sim 10\%$ for ACC) were identified by their 1. significantly higher firing rate, 2. smaller area under peak normalized by peak amplitude, and 3. more

symmetrical ratio of peak amplitude to trough amplitude (Courtin et al., 2014; Middleton et al., 2018), which formed a clearly separable cluster from the rest of the cells in a three-dimensional plot on the axes. The putative interneurons were excluded from subsequent analyses and only the putative pyramidal neurons were used for all the analyses.

LFP power analysis

All LFP and spike analyses were performed with MATLAB (Mathworks) using custom-written scripts. For LFP analyses, a tetrode that was located closest to the center of each of CA1, ACC and BLA was selected for each animal based on histology after the experiment and the same tetrodes were used across all sessions. Timestamps of non-freezing and freezing periods were aligned with those of LFP data by referencing them to the TTL pulse sent from FreezeFrame to Cheetah Software (Neuralynx) at the beginning of the experiment. Power spectral density was calculated across the frequency range 1-200 Hz with the `pmtm` function in MATLAB (Mathworks) using 1.28 s epochs from non-freezing and freezing periods, respectively. Mean power across theta (6-12 Hz), slow-gamma (30-50 Hz) and fast-gamma (60-90 Hz) frequency ranges were then calculated and normalized by the power recorded in the habituation box at the beginning of each experimental day.

LFP-LFP instantaneous amplitude correlation analysis

Correlation of the instantaneous amplitude of LFP oscillations between two regions was analyzed as previously described (Adhikari et al., 2010). First, the raw LFP from the two regions of interest was filtered for the target frequency range using a zero-phase-delay filter and the amplitude envelope was extracted with the Hilbert transform. The correlation coefficient between the two envelopes within the state being analyzed (non-freezing / freezing) was then calculated. To confirm that the observed correlation was not due to spurious coupling, 1.28 s epochs of LFP envelopes were randomly shuffled within each state over the 10 min session only for one of the regions and the correlation was calculated. This process was repeated 1,000 times and the results were averaged. This mean correlation value was then subtracted from the observed correlation to obtain the baseline adjusted correlation.

To calculate the frequency-correlation curve, LFPs of the two regions were filtered with a 4 Hz-wide band-pass filter and correlation was calculated as above. This filter was slid between 4 and 118 Hz with 1 Hz step to obtain correlation values over the entire frequency range.

To analyze the directionality of LFP amplitude between two regions, LFP from one of the regions was shifted in the range of -80 to +80 ms in 5 ms steps and amplitude correlation was calculated for each lag as described above. Peak correlation was considered significant when it exceeded 95 percentile of correlation values obtained by the random shuffling described above and when it resided in the middle of lag range (-70 to +70 ms). Only the mice which showed lag values resulting in significant peak correlations were included in the analysis.

To analyze the time course of LFP correlation at the periods surrounding the onset of freezing, the episodes that include at least 3.2 s of non-freezing periods followed by at least 1.28 s of freezing periods were extracted. To analyze the periods surrounding the offset of freezing, the episodes including at least 1.28 s of freezing periods followed by at least 3.2 s of non-freezing periods were extracted. Within these 4.48 s segments, LFP correlation and lag values were calculated every 0.32 s as described above and averaged over all segments for each time point.

LFP-LFP phase difference analysis

Phase relationship of LFP oscillation between two regions was analyzed by first filtering raw LFP from both regions for the target frequency range. Then, the phase of the filtered LFP was computed using the Hilbert transform. Phase difference between the regions was then calculated during the state being analyzed.

LFP-LFP Granger causality analysis

Granger causality between LFPs from two regions was analyzed using the Multivariate Granger Causality (MVGC) toolbox (Barnett and Seth, 2014). The LFP signal was further down-sampled to 400 Hz and fit to a vector autoregressive model with the model order of 40 (100 ms), which almost corresponded to the range of ACC-CA1 lag that we scanned (-80 to +80 ms) for finding maximum LFP instantaneous amplitude correlation (described above). Spectrally-resolved Granger causality was then obtained and the causality values over the theta frequency range (6-12 Hz) were averaged.

LFP-LFP cross-frequency coupling analysis

Cross-frequency phase-amplitude coupling of LFP oscillation within and between regions was analyzed as previously described (Tort et al., 2010). First, raw LFP from one region was filtered at theta frequency (6-12 Hz), and the phase of the filtered LFP was computed using the Hilbert transform. Raw LFP from the same or different region was also filtered at either slow-gamma (30-50 Hz) or fast-gamma (60-90 Hz) frequency, and the amplitude envelope was extracted with the Hilbert transform. To examine the coupling strength of gamma amplitude to theta phase, theta phases were binned into 36 bins (0-360°, 10° intervals) and the mean amplitude of gamma in each phase bin during the state being analyzed was calculated. These values were then used to calculate the modulation index (Tort et al., 2010), which indicates the modulation strength on gamma amplitude by theta phase.

To generate a comodulogram between low-frequency phase and high-frequency amplitude, the phase of the low-frequency oscillation was extracted between 4 and 18 Hz with bandpass filters of 4 Hz width (stepping by 0.5 Hz) and the amplitude of

high-frequency oscillation was calculated between 25 and 135 Hz with bandpass filters of 10 Hz width (stepping by 2 Hz). Modulation index for each phase-amplitude pair was plotted as a heatmap.

LFP-spike phase-locking analysis

For the analysis using spike data, all the tetrodes placed in each region, including the one used for LFP analysis, were used to maximize the number of units that can be analyzed. Phase-locking of spike activity in one region to LFP oscillation of the same or different region was analyzed either during non-freezing or freezing periods. First, raw LFP was filtered at theta frequency (6–12 Hz) and the phase of the filtered LFP was computed using the Hilbert transform. Each spike was then assigned its corresponding theta phase. Statistical significance of phase-locking was assessed by Rayleigh test for circular uniformity. Strength of phase-locking was quantified by the mean resultant length (MRL), which is the sum of the unit vectors representing the spike phases divided by the number of spikes (Middleton and McHugh, 2016; Sigurdsson et al., 2010). Since MRL is affected by the number of spikes used for analysis (Sigurdsson et al., 2010), 100 spikes were randomly subsampled from each cell to calculate MRL, and mean MRL over 1,000 subsamplings was used as the final result. Cells with less than 100 spikes during the state being analyzed were excluded from analysis.

Co-firing analysis

Co-firing of CA1 neurons either during non-freezing or freezing periods was quantified in two different ways. First, a co-firing index (CFI) was calculated as previously described (Bair et al., 2001; Tamura et al., 2017), which is defined as:

$$\text{CFI} = \frac{C_{12}}{T\sqrt{f_1 f_2}}$$

where C_{12} is a count of co-occurrence of spikes from neurons 1 and 2 within the specified interval, T is the duration of the period being analyzed, and f_1 and f_2 are the mean firing rates (in spikes per second) of neurons 1 and 2. For maximum spike interval, 10 ms was used for all the analyses unless otherwise described. Since this co-firing index is apparently still affected by absolute firing rate of the two neurons, a shift-predictor was subtracted (Bair et al., 2001) in the following way. First, spike latency from the beginning of 1.28 s non-freezing / freezing epochs was randomly shuffled among epochs for only one of the neurons, and co-firing index was calculated. This process was repeated 1,000 times and the mean co-firing index was subtracted from the raw value without shuffling, which generated an index reflecting ‘pure’ spike synchrony. This shuffle-subtracted index is shown in all figures unless otherwise described.

To avoid detecting spurious co-firing due to spike misclassification (Quirk and Wilson, 1999), we confirmed the results by two approaches (Figure S6B). First, the spike interval was limited to 2 ms, in which case burst firing of the same neuron would not cause spurious co-firing when falsely classified as two different neurons. Second, neurons showing more than 0.5% of inter-spike intervals shorter than 2 ms were removed from analysis to avoid using the units potentially containing spikes from more than one neuron.

As an independent measure of co-firing, correlation of binned spike counts (bin size = 10 ms) between two neurons was examined (Livneh and Paz, 2012; Remondes and Wilson, 2013). This method generated almost identical results to those obtained by co-firing index described above when epoch-shuffled values were subtracted. In both cases, neuron pairs with less than 200 spikes for either neuron during the state being analyzed were excluded from analysis.

Place cell analysis

Analysis of place cells in CA1 was performed as described previously (Tanaka et al., 2018) with modifications. First, spikes from each neuron were assigned to 1 cm x 1 cm spatial bins. Then the number of spikes for each bin was divided by the occupancy time of that bin. Finally, they were smoothed with a 1 SD Gaussian kernel. For visualization purpose, images in the figures were further smoothed with 7 spatial bins. Mean firing rates were calculated by averaging the firing rate of each neuron when the velocity of the mouse exceeded 2 cm/s. Peak firing rates were defined as rate in the spatial bin having the maximal value. Place field size was calculated by summing the number of spatial bins where a neuron’s firing rate exceeded 20% of its peak rate. Spatial information was calculated as previously described (Skaggs et al., 1993). Neurons with less than 50 spikes were excluded from analysis.

Ripple detection

Detection of sharp-wave ripple events in CA1 was performed as described previously (Boehringer et al., 2017) with modifications. LFP of CA1 was first filtered between 100–250 Hz using FIR zero-phase shift filter. The amplitude envelope was obtained with the Hilbert transform and then smoothed with 5 ms Gaussian window. Candidate ripple events were extracted as periods where amplitude exceeded 1 standard deviation (SD) above the mean for > 30 ms (which determined the beginning and end of each ripple event) and the peak amplitude within this window exceeded 3 SD above the mean. To select the true ripple events, multi-unit activity (MUA) recorded from CA1 in the same session was converted to instantaneous firing rate, smoothed and checked whether it exceeded 3 SD above the mean during each candidate ripple event to see if there was a concurrent burst firing. Candidate ripple events not coincident with MUA burst firing were excluded from analysis.

Support vector machine (SVM) analysis

The SVM training and classification were performed following previously described methods (Ecker et al., 2010; Hung et al., 2005; Kamitani and Tong, 2005). For within-subject decoding, the time course of LFP instantaneous amplitude correlation between ACC and CA1 was first calculated for different frequencies over the 10 min recent and remote recall sessions. The time course of correlation was then divided into multiple 40 s epochs during non-freezing periods. Correlation values during all epochs from recent and remote sessions except for one epoch from either session were used to train a classifier ('leave-one-out' method (Ecker et al., 2010; Kamitani and Tong, 2005)) using the `svmtrain` function in MATLAB with a linear kernel. The removed epoch was then classified as coming either from recent or remote session using the `svmclassify` function, based on its correlation information. This process was repeated by removing each of all epochs from the two sessions, and the mean classification accuracy was calculated for each mouse. As a control, a classifier was generated by data with class labels (recent / remote) randomly shuffled for each epoch removal, and the mean classification accuracy was calculated over all epoch removals. This procedure was repeated 1,000 times and the mean accuracy was obtained. The accuracy values from the observed and shuffled data were then averaged over mice, respectively, for statistical comparisons among different input datasets.

For between-subject decoding, ACC-CA1 LFP instantaneous amplitude correlation during non-freezing periods of the entire 10 min session was used as a representative value from each mouse. The correlation values during recent and remote sessions were first normalized by those during the baseline session for each mouse to reduce variability. Correlation values for recent and remote sessions from all mice except one mouse were used to train a classifier, and the two sessions from the removed mouse were classified as either recent or remote session. This process was repeated by removing each of all mice and the mean classification accuracy was calculated over all mouse removals. As a control, accuracy was calculated using a classifier generated by data with class labels (recent / remote) randomly shuffled. This procedure was repeated 1,000 times and 95 percentile of the accuracy values was obtained, which was then compared with the observed accuracy to test its statistical significance.

For decoding by spike activity, the phase-locking strength (MRL) of CA1 neurons to ACC theta, firing rate of CA1 neurons and co-firing between CA1 neuron pairs over the entire 10 min session were used as an input. These values from all neurons / neuron pairs coming from all mice recorded at recent and remote sessions, except one neuron / neuron pair, were used to train a classifier. The removed neuron / neuron pair was then classified as coming either from recent or remote session. This process was repeated by removing each of all neurons / neuron pairs and the mean classification accuracy was calculated over all removals. Statistical significance of the accuracy was tested as described above. For some of the analyses, only the neurons / neuron pairs with top 20 or 10 percent of firing rate / co-firing values within each of recent and remote sessions, respectively, were used as an input.

Statistics

All statistical tests were performed either by MATLAB, SPSS (IBM) or Excel (Microsoft) with custom-written scripts. A two-tailed within-subject t test was used to compare a measure between two different sessions. A within-subject one-way ANOVA was used to compare a measure among three sessions, followed by a post hoc pairwise comparison with Tukey's HSD test. Alternatively, a two-tailed between-subject t test or a between-subject one-way ANOVA with post hoc pairwise comparison by Tukey's HSD test was used if it is not a repeated-measure (such as co-firing index from different neuronal pairs). For measures that do not follow normal distribution (such as firing rate and phase-locking MRL), a two-tailed Mann-Whitney test or a Kruskal-Wallis test with post hoc pairwise comparison by Steel-Dwass test was used. A test of no correlation (correlation t test) was used for testing significance of correlation between different measures. Other specialized statistical tests (such as Rayleigh test and permutation test) were performed as described in the relevant method sections. All the statistically significant differences with $p < 0.05$ are described in each figure with different significance levels indicated by asterisks as * $p < 0.05$, ** $p < 0.01$, *** $p < 0.001$. All bar graphs and line plots show mean \pm SEM. In all box plots, the middle, bottom and top lines correspond to the median, lower and upper quartiles, and the edges of lower and upper whiskers correspond to the 5th and 95th percentiles, respectively.

DATA AND CODE AVAILABILITY

Custom MATLAB scripts developed for the analyses of the *in vivo* electrophysiological data are described in detail above. All custom scripts and data contained in this manuscript are available upon request from the Lead Contact, Thomas J. McHugh (thomas.mchugh@riken.jp).

Cell Reports, Volume 29

Supplemental Information

**Physiological Signature of Memory Age
in the Prefrontal-Hippocampal Circuit**

Yuichi Makino, Denis Polygalov, Federico Bolaños, Andrea Benucci, and Thomas J. McHugh

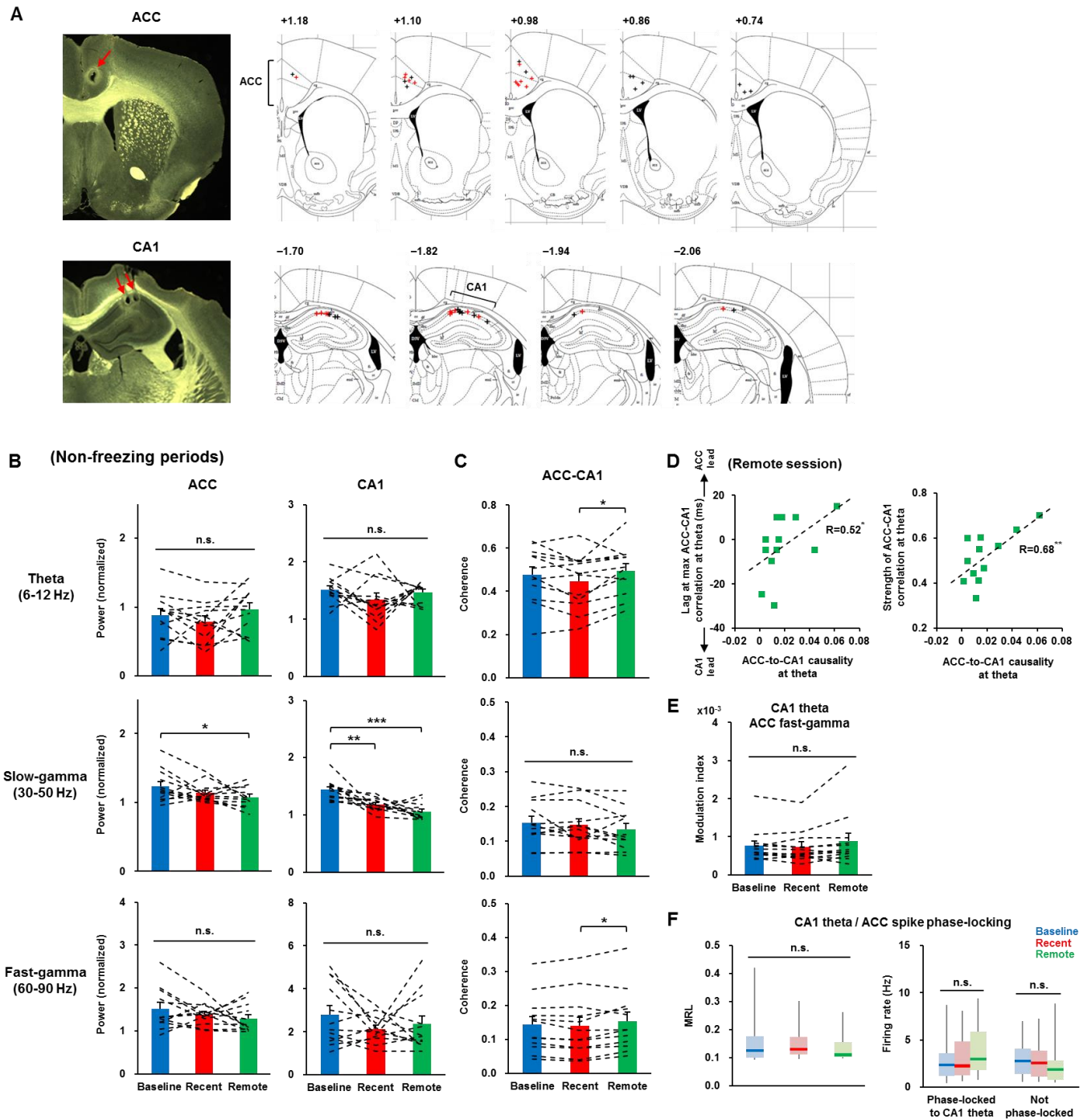


Figure S1 (related to Figures 1-3). ACC-CA1 Synchrony at Theta and Fast-gamma Frequency, but not the Oscillatory Power within Regions, is Enhanced During the Remote Recall Session

(A) Location of tetrode tips in ACC and CA1 was verified by making electrolytic lesions after recordings. Left: representative image with a lesion (indicated by an arrow) is shown. Right: tetrode locations for all mice recorded ($n = 12$) are reconstructed on coronal sections with the distance from bregma shown on the top (Paxinos & Franklin, 2001). Red crosses indicate the tetrodes that were used for both LFP and spike analyses, and black crosses indicate the tetrodes used only for spike analysis.

(B) Oscillatory power over each of theta, slow-gamma and fast-gamma frequency ranges during non-freezing periods is shown for baseline, recent and remote session, and for ACC and CA1, respectively (theta, ACC: $F_{2,22} = 1.57$, $p = 0.230$; theta, CA1: $F_{2,22} = 1.08$, $p = 0.356$; slow-gamma, ACC: $F_{2,22} = 3.56$, $p = 0.046$; baseline vs recent, $p = 0.274$; baseline vs remote, $p = 0.038$; recent vs remote, $p = 0.544$; slow-gamma, CA1: $F_{2,22} = 19.41$, $p < 0.001$; baseline vs recent, $p = 0.001$;

baseline vs remote, $p < 0.001$; recent vs remote, $p = 0.162$; fast-gamma, ACC: $F_{2,22} = 1.59$, $p = 0.227$; fast-gamma, CA1: $F_{2,22} = 1.72$, $p = 0.202$). Power was normalized by that during the habituation session performed on the same day.

(C) Coherence of LFP between ACC and CA1 was calculated during non-freezing periods and averaged over theta, slow-gamma and fast-gamma frequency ranges, respectively (theta: $F_{2,22} = 4.50$, $p = 0.023$; baseline vs recent, $p = 0.170$; baseline vs remote, $p = 0.529$; recent vs remote, $p = 0.019$; slow-gamma: $F_{2,22} = 2.38$, $p = 0.116$; fast-gamma: $F_{2,22} = 3.64$, $p = 0.043$; baseline vs recent, $p = 0.745$; baseline vs remote, $p = 0.168$; recent vs remote, $p = 0.040$).

(D) Left: correlation between Granger causality from ACC to CA1 at theta frequency with the ACC-CA1 time lag resulting in the max theta instantaneous amplitude correlation over individual mice ($R = 0.52$, $p = 0.042$). Right: correlation between Granger causality from ACC to CA1 at theta frequency with the strength of ACC-CA1 theta instantaneous amplitude correlation ($R = 0.68$, $p = 0.007$).

(E) Strength of cross-frequency modulation by CA1 theta phase on ACC fast-gamma amplitude during non-freezing periods ($F_{2,22} = 2.17$, $p = 0.138$).

(F) Left: MRL of ACC neurons that are significantly phase-locked to CA1 theta (Rayleigh test, $p < 0.05$) during non-freezing periods ($n = 48$ [baseline], 46 [recent], and 36 [remote] neurons; $H = 1.10$, $p = 0.577$). Right: firing rates during non-freezing periods of the ACC neurons that are and are not phase-locked to CA1 theta (phase-locked: $n = 48$ [baseline], 46 [recent], and 36 [remote] neurons; $H = 2.82$, $p = 0.244$; not phase-locked: $n = 28$ [baseline], 45 [recent], and 23 [remote] neurons; $H = 2.07$, $p = 0.355$).

In (B), (C), and (E), $n = 12$ mice for all comparisons, within-subject ANOVA with post-hoc comparisons by Tukey's HSD test. In (D), $n = 12$ mice, test of no correlation. In (F), Kruskal-Wallis test, neurons recorded from 13 (baseline), 13 (recent), and 12 (remote) mice. For all bar graphs, data are represented as mean \pm SEM, and dotted lines indicate values from individual mice. For all box plots, the middle, bottom and top lines correspond to the median, lower and upper quartiles, and the edges of lower and upper whiskers correspond to the 5th and 95th percentiles, respectively. * $p < 0.05$, ** $p < 0.01$, and *** $p < 0.001$.

(Freezing periods)

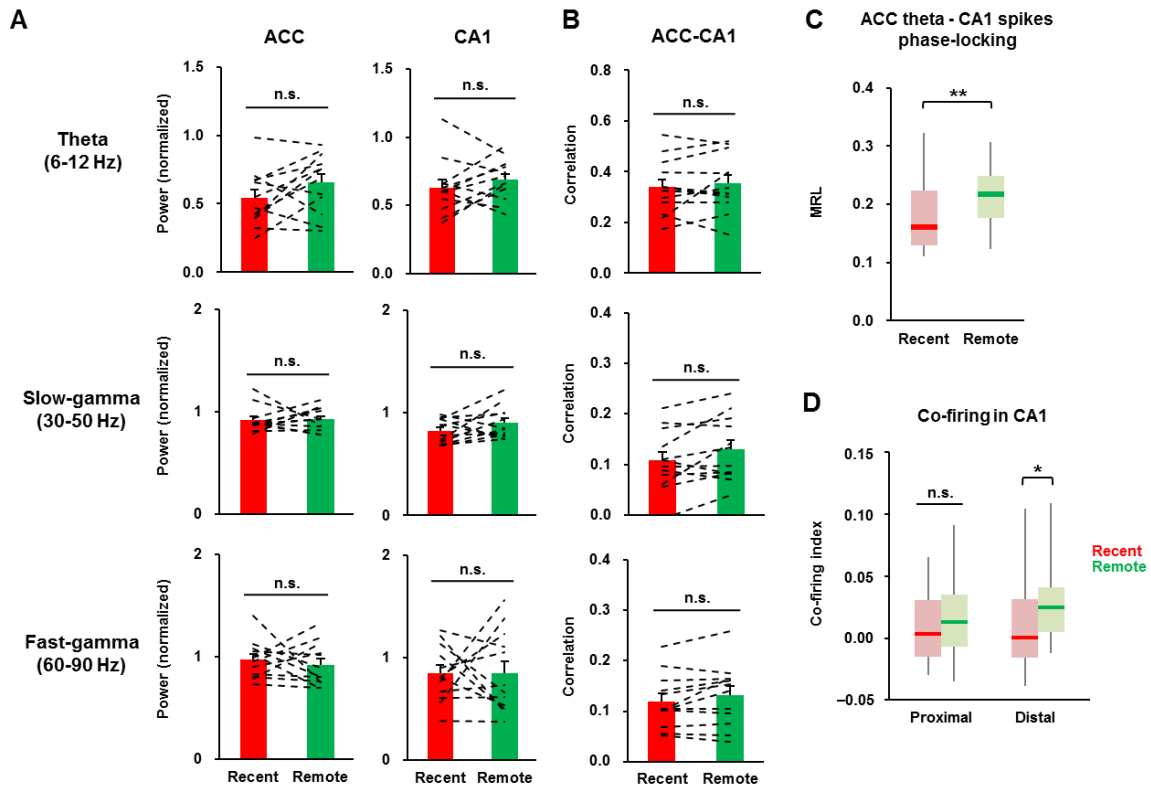


Figure S2 (related to Figures 1-4). ACC Entrainment on CA1 Firing and CA1 Distal Co-firing is Enhanced during Freezing During the Remote Recall Session

(A) Oscillatory power over each of theta, slow-gamma and fast-gamma frequency ranges during freezing periods is shown for baseline, recent and remote session, and for ACC and CA1, respectively (theta, ACC: $t_{11} = 1.71$, $p = 0.115$; theta, CA1: $t_{11} = 1.10$, $p = 0.295$; slow-gamma, ACC: $t_{11} = 0.07$, $p = 0.948$; slow-gamma, CA1: $t_{11} = 1.59$, $p = 0.140$; fast-gamma, ACC: $t_{11} = 0.58$, $p = 0.571$; fast-gamma, CA1: $t_{11} = 0.05$, $p = 0.964$). Power was normalized by that during the habituation session performed on the same day.

(B) Instantaneous amplitude correlations between ACC and CA1 at theta, slow-gamma and fast-gamma during freezing periods (theta: $t_{11} = 0.75$, $p = 0.468$; slow-gamma: $t_{11} = 2.20$, $p = 0.050$; fast-gamma: $t_{11} = 1.79$, $p = 0.102$).

(C) MRL of CA1 neurons that are significantly phase-locked to ACC theta during freezing periods ($n = 45$ [recent] and 50 [remote] neurons; $U = 744$, $p = 0.004$).

(D) Co-firing for CA1 neuron pairs recorded from the same (proximal) or different (distal) tetrodes during freezing periods (proximal: $n = 87$ [recent] and 49 [remote] neuron pairs; $t_{134} = 1.28$, $p = 0.202$; distal: $n = 68$ [recent] and 27 [remote] neuron pairs; $t_{93} = 2.07$, $p = 0.041$).

In (A) and (B), $n = 12$ mice, two-tailed within-subject t-test. In (C), two-tailed Mann-Whitney test, neurons recorded from 13 (recent) and 12 (remote) mice. In (D), two-tailed between-subject t-test, neurons recorded from 13 (recent) and 12 (remote) mice. For all bar graphs, data are represented as mean \pm SEM, and dotted lines indicate values from individual mice. For all box plots, the middle, bottom and top lines correspond to the median, lower and upper quartiles, and the edges of lower and upper whiskers correspond to the 5th and 95th percentiles, respectively. * $p < 0.05$ and ** $p < 0.01$.

(Habituation sessions)

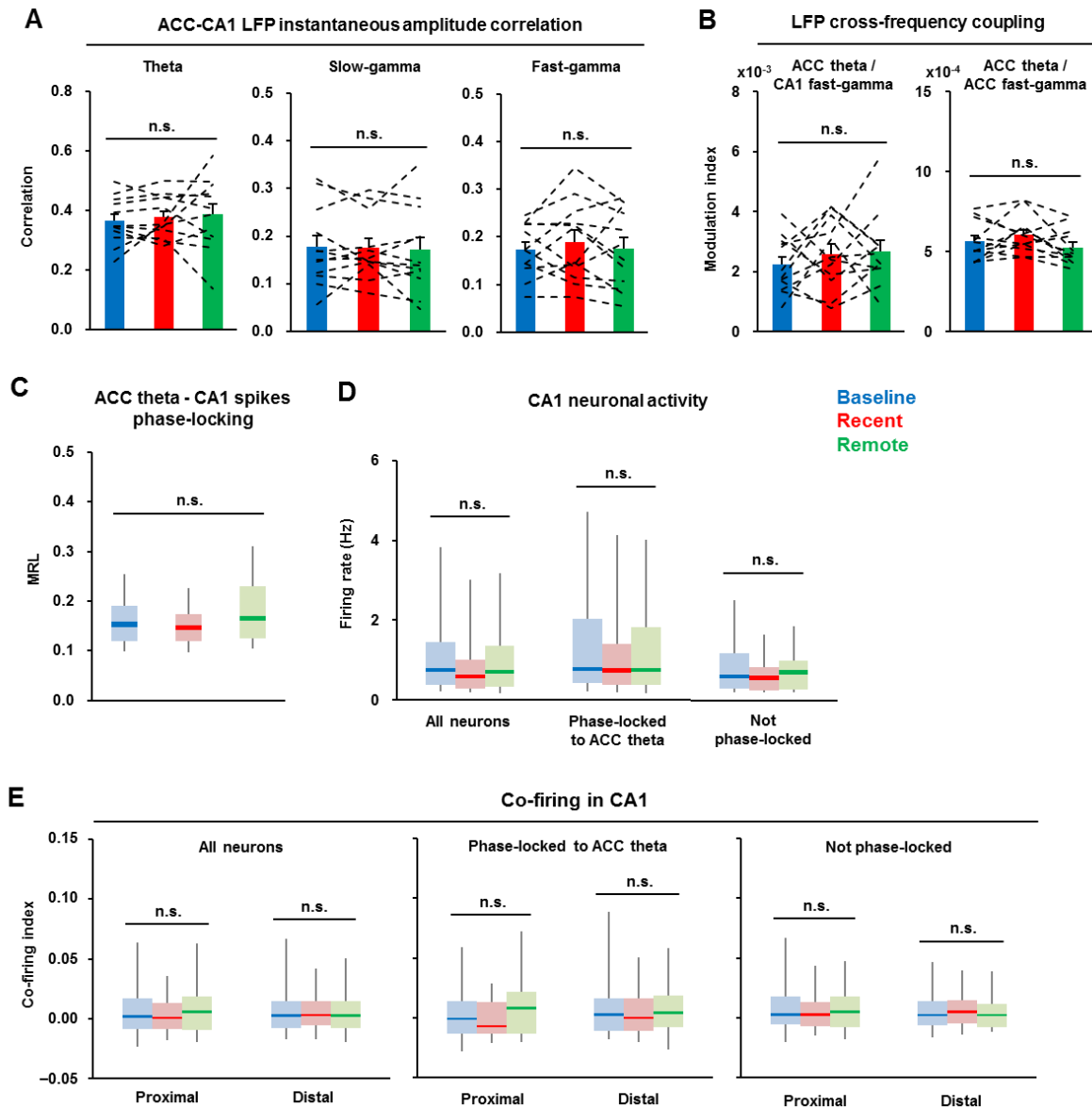


Figure S3 (related to Figures 1-4). No Time-dependent Changes Are Seen during Habituation

(A) Instantaneous amplitude correlation between ACC and CA1 was calculated for each frequency range during the 10 min habituation session performed 30 min before each of baseline, recent and remote session. Correlation was comparable among all sessions for theta ($F_{2,22} = 0.25$, $p = 0.778$), slow-gamma ($F_{2,22} = 0.13$, $p = 0.875$) and fast-gamma ($F_{2,22} = 0.53$, $p = 0.594$).

(B) Strength of cross-frequency modulation by ACC theta on CA1 fast-gamma and ACC fast-gamma were both comparable among all sessions (CA1 fast-gamma: $F_{2,22} = 0.70$, $p = 0.509$; ACC fast-gamma: $F_{2,22} = 2.69$, $p = 0.090$).

(C) Phase-locking strength (MRL) of CA1 neurons that were significantly phase-locked to ACC theta (Rayleigh test, $p < 0.05$) were comparable among all sessions ($n = 85$ [baseline], 65 [recent], and 55 [remote] neurons; $H = 3.85$, $p = 0.146$).

(D) Firing rates of the entire CA1 neuronal populations as well as of the subpopulations that were and were not phase-locked to ACC theta were all comparable among all sessions (all neurons: $n = 140$ [baseline], 141 [recent], and 100 [remote] neurons; $H = 5.47$, $p = 0.065$; phase-locked: $n = 85$ [baseline], 65 [recent], and 55 [remote] neurons; $H = 1.35$, $p = 0.510$; not phase-locked: $n = 55$ [baseline], 76 [recent], and 45 [remote] neurons; $H = 3.04$, $p = 0.219$).

(E) Co-firing index of CA1 neuron pairs (spike interval < 10 msec, raw minus epoch-shuffled) was comparable among all sessions for both proximal and distal pairs and for the entire CA1 population as well as for the subpopulations that were

and were not phase-locked to ACC theta (all neurons and proximal: $n = 272$ [baseline], 222 [recent], and 160 [remote] neuron pairs; $F_{2,651} = 2.10$, $p = 0.124$; all neurons and distal: $n = 225$ [baseline], 194 [recent], and 130 [remote] neuron pairs; $F_{2,546} = 0.68$, $p = 0.508$; phase-locked and proximal: $n = 111$ [baseline], 56 [recent], and 60 [remote] neuron pairs; $F_{2,224} = 1.84$, $p = 0.161$; phase-locked and distal: $n = 90$ [baseline], 63 [recent], and 45 [remote] neuron pairs; $F_{2,195} = 1.08$, $p = 0.342$; not phase-locked and proximal: $n = 161$ [baseline], 166 [recent], and 100 [remote] neuron pairs; $F_{2,424} = 1.01$, $p = 0.365$; not phase-locked and distal: $n = 135$ [baseline], 131 [recent], and 85 [remote] neuron pairs; $F_{2,348} = 0.31$, $p = 0.732$). In (A) and (B), $n = 12$ mice, within-subject ANOVA. In (C) and (D), Kruskal-Wallis test, neurons recorded from 13 (baseline), 13 (recent), and 12 (remote) mice. In (E), between-subject ANOVA, neurons recorded from 13 (baseline), 13 (recent), and 12 (remote) mice. For all bar graphs, data are represented as mean \pm SEM, and dotted lines indicate values from individual mice. For all box plots, the middle, bottom and top lines correspond to the median, lower and upper quartiles, and the edges of lower and upper whiskers correspond to the 5th and 95th percentiles, respectively.

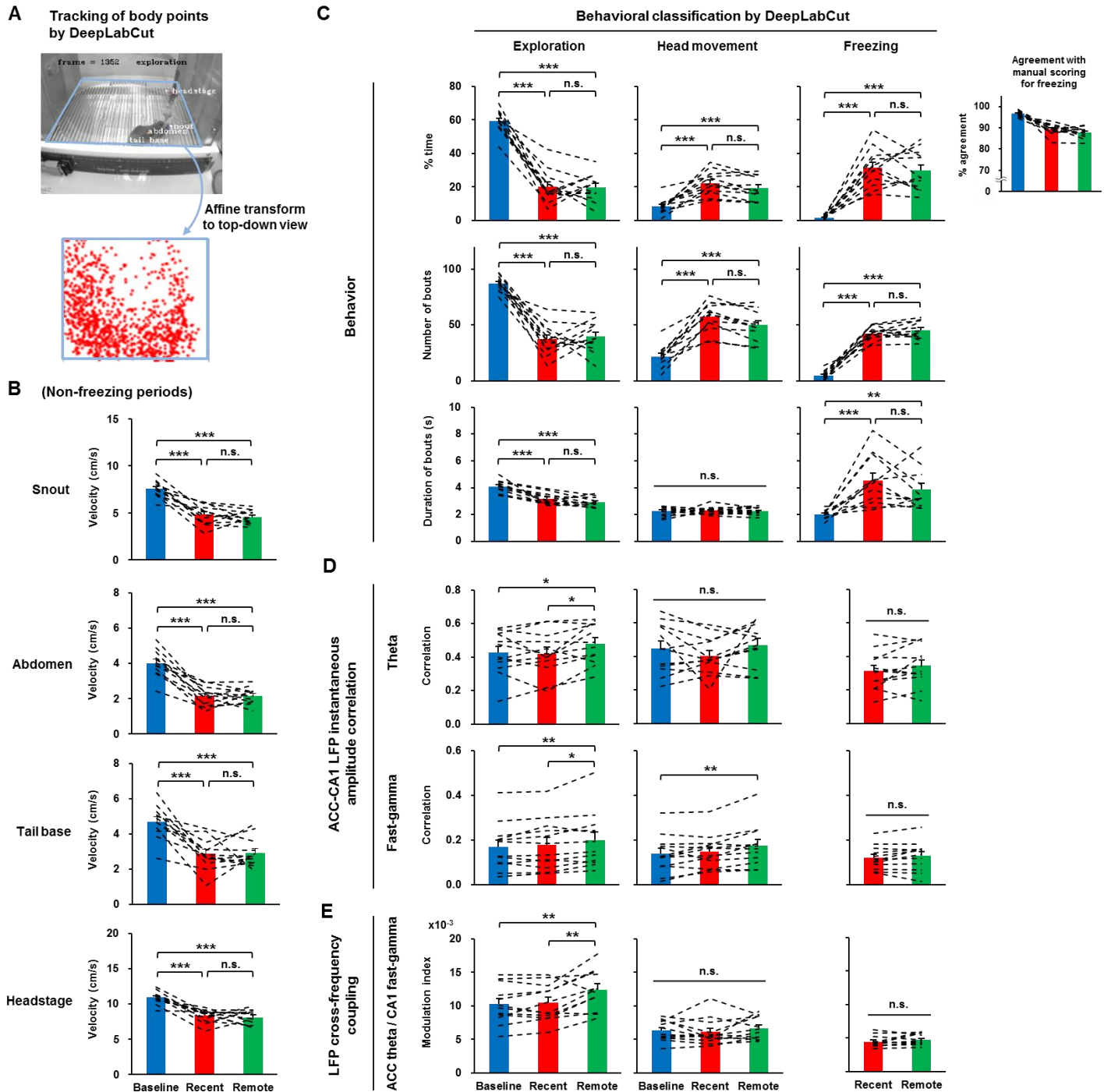


Figure S4 (related to Figures 1-2). Enhanced ACC-CA1 Synchrony at the Remote Session is Independent of Non-freezing Behavior Classified by DeepLabCut

(A) Representative picture of automated body point tracking, in which each body point (snout, abdomen, tail base and headstage) is indicated by dots of different colors. The classified behavioral state (exploration, head movement or freezing) is indicated at the top. The coordinates from the angled view were converted to those from the top-down view by affine transformation.

(B) Velocity of each body point during non-freezing periods (snout: $F_{2,22} = 37.95$, $p < 0.001$; baseline vs recent, $p < 0.001$; baseline vs remote, $p < 0.001$; recent vs remote, $p = 0.756$; abdomen: $F_{2,22} = 50.27$, $p < 0.001$; baseline vs recent, $p < 0.001$; baseline vs remote, $p < 0.001$; recent vs remote, $p = 0.994$; tail base: $F_{2,22} = 20.54$, $p < 0.001$; baseline vs recent, $p < 0.001$; baseline vs remote, $p < 0.001$; recent vs remote, $p = 0.971$; headstage: $F_{2,22} = 29.83$, $p < 0.001$; baseline vs recent, $p < 0.001$; baseline vs remote, $p < 0.001$; recent vs remote, $p = 0.833$).

(C) Percent time, number of bouts (continuous episodes) per session and mean duration of bouts under each behavioral state classified by DeepLabCut (% time, exploration: $F_{2,22} = 100.35$, $p < 0.001$; baseline vs recent, $p < 0.001$; baseline vs remote, $p < 0.001$; recent vs remote, $p = 0.988$; % time, head movement: $F_{2,22} = 28.47$, $p < 0.001$; baseline vs recent, $p < 0.001$; baseline vs remote, $p < 0.001$; recent vs remote, $p = 0.246$; % time, freezing: $F_{2,22} = 45.71$, $p < 0.001$; baseline vs recent, $p < 0.001$; baseline vs remote, $p < 0.001$; recent vs remote, $p = 0.849$; number of bouts, exploration: $F_{2,22} = 64.29$, $p < 0.001$; baseline vs recent, $p < 0.001$; baseline vs remote, $p < 0.001$; recent vs remote, $p = 0.879$; number of bouts, head movement: $F_{2,22} = 58.66$, $p < 0.001$; baseline vs recent, $p < 0.001$; baseline vs remote, $p < 0.001$; recent vs remote, $p = 0.108$; number of bouts, freezing: $F_{2,22} = 138.04$, $p < 0.001$; baseline vs recent, $p < 0.001$; baseline vs remote, $p < 0.001$; recent vs remote, $p = 0.599$; duration of bouts, exploration: $F_{2,22} = 35.78$, $p < 0.001$; baseline vs recent, $p < 0.001$; baseline vs remote, $p < 0.001$; recent vs remote, $p = 0.179$; duration of bouts, head movement: $F_{2,22} = 0.11$, $p = 0.901$; duration of bouts, freezing: $F_{2,20} = 11.96$, $p < 0.001$; baseline vs recent, $p < 0.001$; baseline vs remote, $p = 0.007$; recent vs remote: $p = 0.440$). The inset shows % agreement with manual scoring (Figure 1B) for freezing.

(D) Instantaneous amplitude correlation between ACC and CA1 at theta and fast-gamma during each behavioral state (theta, exploration: $F_{2,22} = 4.90$, $p = 0.017$; baseline vs recent, $p = 0.963$; baseline vs remote, $p = 0.044$; recent vs remote, $p = 0.025$; theta, head movement: $F_{2,22} = 2.06$, $p = 0.151$; theta, freezing: $t_{11} = 1.43$, $p = 0.179$; fast-gamma, exploration: $F_{2,22} = 7.50$, $p = 0.003$; baseline vs recent, $p = 0.479$; baseline vs remote, $p = 0.003$; recent vs remote, $p = 0.041$; fast-gamma, head movement: $F_{2,22} = 6.20$, $p = 0.007$; baseline vs recent, $p = 0.593$; baseline vs remote, $p = 0.007$; recent vs remote, $p = 0.059$; fast-gamma, freezing: $t_{11} = 1.25$, $p = 0.238$).

(E) Strength of cross-frequency modulation by ACC theta phase on CA1 fast-gamma amplitude during non-freezing periods (exploration: $F_{2,22} = 10.06$, $p = 0.001$; baseline vs recent, $p = 0.913$; baseline vs remote, $p = 0.002$; recent vs remote, $p = 0.004$; head movement: $F_{2,22} = 0.70$, $p = 0.508$; freezing: $t_{11} = 1.27$, $p = 0.232$).

In (B)-(E), $n = 12$ mice, within-subject ANOVA with post-hoc comparisons by Tukey's HSD test for comparing three sessions, and two-tailed within-subject t-test for comparing two sessions. For all bar graphs, data are represented as mean \pm SEM, and dotted lines indicate values from individual mice. * $p < 0.05$, ** $p < 0.01$, and *** $p < 0.001$.

Figure S5 (related to Figures 1-3). Enhanced ACC-CA1 Interaction at the Remote Session is Independent of Movement Velocity and CA1 Spatial Coding

(A) Distribution of percent time during which mice spent under each velocity range (1 cm/s bin) during non-freezing periods, which was tracked by the location of LEDs on mouse head at 30 Hz.

(B) Mean velocity during non-freezing periods ($F_{2,22} = 12.16$, $p < 0.001$; baseline vs recent: $p = 0.012$; baseline vs remote, $p < 0.001$; recent vs remote, $p = 0.234$).

(C) Instantaneous amplitude correlation between ACC and CA1 at theta and fast-gamma during non-freezing periods (theta, 0-5 cm/s: $F_{2,22} = 2.82$, $p = 0.081$; theta, 5-10 cm/s: $F_{2,22} = 6.18$, $p = 0.007$; baseline vs recent, $p = 0.660$; baseline vs remote, $p = 0.007$; recent vs remote, $p = 0.050$; theta, 10-15 cm/s: $F_{2,22} = 7.71$, $p = 0.003$; baseline vs recent, $p = 0.982$; baseline vs remote, $p = 0.006$; recent vs remote, $p = 0.009$; theta, 15-20 cm/s: $F_{2,22} = 5.55$, $p = 0.011$; baseline vs recent, $p = 0.997$; baseline vs remote, $p = 0.021$; recent vs remote, $p = 0.025$; theta, 20- cm/s: $F_{2,22} = 5.22$, $p = 0.014$; baseline vs recent, $p = 0.981$; baseline vs remote, $p = 0.034$; recent vs remote, $p = 0.022$; fast-gamma, 0-5 cm/s: $F_{2,22} = 4.69$, $p = 0.020$; baseline vs recent, $p = 0.479$; baseline vs remote, $p = 0.016$; recent vs remote, $p = 0.174$; fast-gamma, 5-10 cm/s: $F_{2,22} = 1.58$, $p = 0.228$; fast-gamma, 10-15 cm/s: $F_{2,22} = 5.90$, $p = 0.009$; baseline vs recent, $p = 0.979$; baseline vs remote, $p = 0.023$; recent vs remote, $p = 0.015$; fast-gamma, 15-20 cm/s: $F_{2,22} = 9.28$, $p = 0.001$; baseline vs recent, $p = 0.752$; baseline vs remote, $p = 0.002$; recent vs remote, $p = 0.009$; fast-gamma, 20- cm/s: $F_{2,22} = 1.56$, $p = 0.232$).

(D) Strength of cross-frequency modulation by ACC theta phase on CA1 fast-gamma amplitude during non-freezing periods (0-5 cm/s: $F_{2,22} = 1.81$, $p = 0.188$; 5-10 cm/s: $F_{2,22} = 3.94$, $p = 0.034$; baseline vs recent, $p = 0.980$; baseline vs remote, $p = 0.072$; recent vs remote, $p = 0.049$; 10-15 cm/s: $F_{2,22} = 0.94$, $p = 0.405$; 15-20 cm/s: $F_{2,22} = 6.25$, $p = 0.007$; baseline vs recent, $p = 0.916$; baseline vs remote, $p = 0.024$; recent vs remote, $p = 0.010$; 20- cm/s: $F_{2,22} = 8.27$, $p = 0.002$; baseline vs recent, $p = 0.641$; baseline vs remote, $p = 0.002$; recent vs remote, $p = 0.018$).

(E) Representative place field maps of CA1 neurons for each session. Firing rate at each spatial location is shown by a heat map along with the peak firing rate for each neuron.

(F) Peak firing rate of neurons ($H = 4.78$, $p = 0.092$).

(G) Mean firing rate of neurons ($H = 2.72$, $p = 0.257$).

(H) Spatial information that each neuron contains ($H = 4.76$, $p = 0.092$). See Skaggs et al. (1993) for the definition.

(I) Place field size of each neuron ($H = 19.59$, $p < 0.001$; baseline vs recent, $p < 0.001$; baseline vs remote, $p = 0.002$; recent vs remote, $p = 0.921$).

In (B)-(D), $n = 12$ mice, within-subject ANOVA with post-hoc comparisons by Tukey's HSD test. In (F)-(I), $n = 141$ (baseline), 129 (recent), and 112 (remote) neurons, Kruskal-Wallis test with post-hoc comparisons by Steel-Dwass test, neurons recorded from 13 (baseline), 13 (recent), and 12 (remote) mice. For all bar graphs, data are represented as mean \pm SEM, and dotted lines indicate values from individual mice. For all box plots, the middle, bottom and top lines correspond to the median, lower and upper quartiles, and the edges of lower and upper whiskers correspond to the 5th and 95th percentiles, respectively. * $p < 0.05$, ** $p < 0.01$, and *** $p < 0.001$.

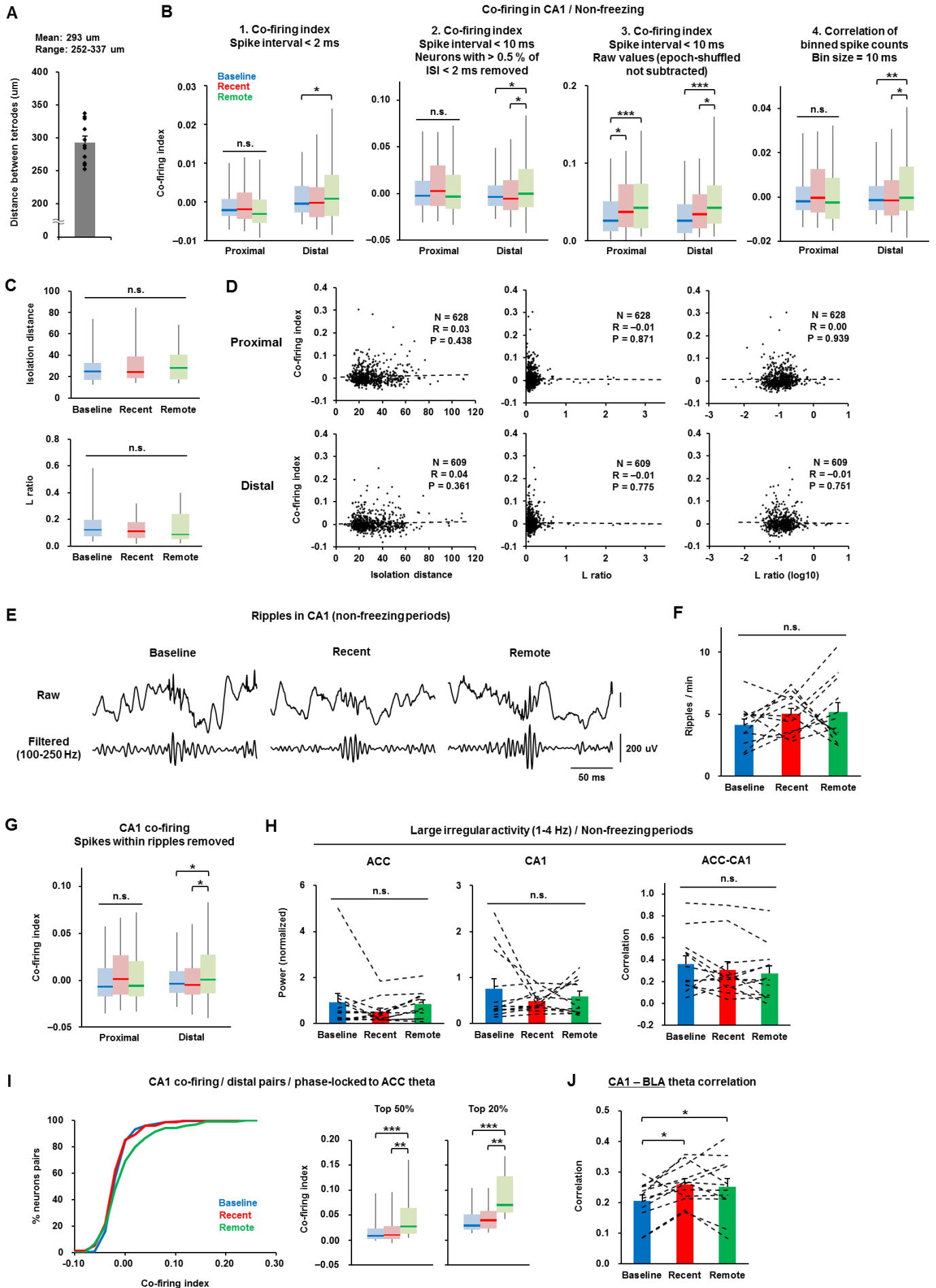


Figure S6 (related to Figure 4). Increased Long-distance Co-firing in CA1 during Remote Recall Session is Observed with Multiple Indices and Does Not Reflect Altered Ripple Events

(A) Distance between the two CA1 tetrodes which was calculated by post-recording lesions.

(B) Co-firing of CA1 proximal and distal neuron pairs during non-freezing periods with different indices (index 1, proximal: $F_{2,625} = 0.55$, $p = 0.577$; index 1, distal: $F_{2,606} = 4.15$, $p = 0.016$; baseline vs recent, $p = 0.999$; baseline vs remote, $p = 0.017$; recent vs remote, $p = 0.067$; index 2, proximal: $F_{2,579} = 1.85$, $p = 0.158$; index 2, distal: $F_{2,567} = 4.54$, $p = 0.011$; baseline vs recent, $p = 0.991$; baseline vs remote, $p = 0.014$; recent vs remote, $p = 0.042$; index 3, proximal: $F_{2,625} = 11.39$, $p < 0.001$; baseline vs recent, $p = 0.028$; baseline vs remote, $p < 0.001$; recent vs remote, $p = 0.225$; index 3, distal: $F_{2,606} = 13.49$, $p < 0.001$; baseline vs recent, $p = 0.208$; baseline vs remote, $p < 0.001$; recent vs remote, $p = 0.014$; index 4, proximal: $F_{2,625} = 0.67$, $p = 0.512$; index 4, distal: $F_{2,606} = 5.57$, $p = 0.004$; baseline vs recent, $p = 0.997$; baseline vs remote, $p = 0.004$; recent vs remote, $p = 0.027$; for index 2, $n = 307$ [baseline], 123 [recent], and 152 [remote] proximal neuron pairs and $n = 291$ [baseline], 121 [recent], and 158 [remote] distal neuron pairs; for all the other indices, $n = 326$ [baseline], 143 [recent], and 159 [remote] proximal neuron pairs and $n = 316$ [baseline], 133 [recent], and 160 [remote] distal neuron pairs). See STAR Methods for calculation of these indices. All of the indices demonstrated similar results except the Index 3, which could be affected by non-specific changes such as altered firing rate (see STAR Methods).

(C) Quality of CA1 single unit isolation indicated by isolation distance and L ratio (Schmitzer-Torbert et al., 2005) (isolation distance: $H = 2.30$, $p = 0.317$; L ratio: $H = 5.60$, $p = 0.061$; $n = 144$ [baseline], 140 [recent], and 115 [remote] neurons).

(D) Correlation of isolation distance and L ratio of CA1 neurons with co-firing of proximal and distal neuron pairs during non-freezing periods. Data from all sessions were pooled.

(E) Representative raw and filtered CA1 LFP at 100-250 Hz around the detected ripple events during non-freezing periods.

(F) Occurrence of CA1 ripple events per minute ($F_{2,22} = 1.00$, $p = 0.384$)

(G) Co-firing of CA1 proximal and distal neuronal pairs when the spikes within ripple events were removed (proximal: $n = 326$ [baseline], 143 [recent], and 159 [remote] neuron pairs; $F_{2,625} = 1.47$, $p = 0.231$; distal: $n = 316$ [baseline], 133 [recent], and 160 [remote] neuron pairs; $F_{2,606} = 4.72$, $p = 0.009$; baseline vs recent, $p = 0.996$; baseline vs remote, $p = 0.011$; recent vs remote, $p = 0.037$).

(H) Oscillatory power of ACC and CA1 LFP as well as ACC-CA1 instantaneous amplitude correlation over large-irregular activity range (1-4 Hz) during non-freezing periods (ACC power: $F_{2,22} = 1.46$, $p = 0.254$; CA1 power: $F_{2,22} = 0.95$, $p = 0.402$; ACC-CA1 correlation: $F_{2,22} = 1.77$, $p = 0.193$).

(I) (Left) Cumulative distribution for co-firing index of CA1 distal neuron pairs that are both phase-locked to ACC theta. (Right) Co-firing index of those neuron pairs with top 50 and 20 percent of index values within each session, respectively (Top 50%: $n = 120$ [baseline], 37 [recent], and 60 [remote] neuron pairs; $F_{2,214} = 12.06$, $p < 0.001$; baseline vs recent, $p = 0.941$; baseline vs remote, $p < 0.001$; recent vs remote, $p = 0.003$; Top 20%: $n = 48$ [baseline], 15 [recent], and 24 [remote] neuron pairs; $F_{2,84} = 11.88$, $p < 0.001$; baseline vs recent, $p = 0.893$; baseline vs remote, $p < 0.001$; recent vs remote, $p = 0.005$).

(J) LFPs were recorded from CA1 and basolateral amygdala (BLA) simultaneously. Instantaneous amplitude correlation at theta frequency between CA1 and BLA over the entire recording session (10 min) was significantly higher during the recent memory and remote memory sessions compared to the baseline session ($F_{2,22} = 5.84$, $p = 0.009$; baseline vs recent, $p = 0.012$; baseline vs remote, $p = 0.034$; recent vs remote, $p = 0.880$).

In (B), (G), and (I), between-subject ANOVA with post-hoc comparisons by Tukey's HSD test, neurons recorded from 13 (baseline), 13 (recent), and 12 (remote) mice. In (C), Kruskal-Wallis test, neurons recorded from 13 (baseline), 13 (recent), and 12 (remote) mice. In (D), test of no correlation, neurons recorded from 13 (baseline), 13 (recent), and 12 (remote) mice. In (F), (H), and (J), $n = 12$ mice, within-subject ANOVA with post-hoc comparisons by Tukey's HSD test. For all bar graphs, data are represented as mean \pm SEM, and dotted lines indicate values from individual mice. For all box plots, the middle, bottom and top lines correspond to the median, lower and upper quartiles, and the edges of lower and upper whiskers correspond to the 5th and 95th percentiles, respectively. * $p < 0.05$, ** $p < 0.01$, and *** $p < 0.001$.